
23 Apr 2024

Li₂MP₂S₆: Building-Block Approach to a Family of 2D Non-van Der Waals-Layered Materials and their Water, Ammonia, and Ion Intercalation Properties

Santhoshkumar Sundaramoorthy

Nikolay Gerasimchuk

Kartik Ghosh

Steven P. Kelley

et. al. For a complete list of authors, see https://scholarsmine.mst.edu/chem_facwork/3781

Follow this and additional works at: https://scholarsmine.mst.edu/chem_facwork

 Part of the [Chemistry Commons](#)

Recommended Citation

S. Sundaramoorthy et al., "Li₂MP₂S₆: Building-Block Approach to a Family of 2D Non-van Der Waals-Layered Materials and their Water, Ammonia, and Ion Intercalation Properties," *Chemistry of Materials*, vol. 36, no. 8, pp. 3574 - 3587, American Chemical Society, Apr 2024.

The definitive version is available at <https://doi.org/10.1021/acs.chemmater.3c02829>

This Article - Journal is brought to you for free and open access by Scholars' Mine. It has been accepted for inclusion in Chemistry Faculty Research & Creative Works by an authorized administrator of Scholars' Mine. This work is protected by U. S. Copyright Law. Unauthorized use including reproduction for redistribution requires the permission of the copyright holder. For more information, please contact scholarsmine@mst.edu.

Li₂MP₂S₆: Building-Block Approach to a Family of 2D Non-van der Waals-Layered Materials and Their Water, Ammonia, and Ion Intercalation Properties

Santhoshkumar Sundaramoorthy, Nikolay Gerasimchuk, Kartik Ghosh, Steven P. Kelley, and Amitava Choudhury*



Cite This: *Chem. Mater.* 2024, 36, 3574–3587



Read Online

ACCESS |



Metrics & More

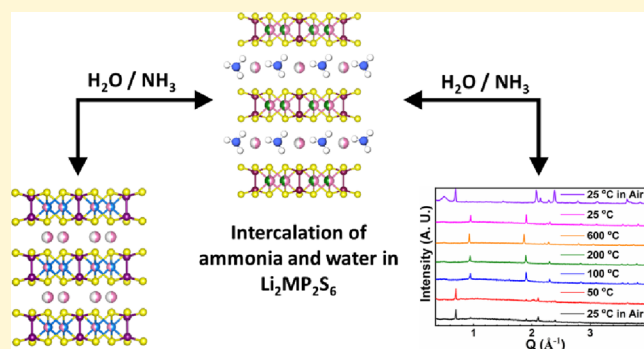


Article Recommendations



Supporting Information

ABSTRACT: A series of non-van der Waals 2D quaternary thiophosphates with nominal composition, Li₂MP₂S₆ (M = V, Mn, Fe, Co, Ni, and Zn), has been successfully synthesized through solid-state metathesis reactions by a building block approach as well as starting with a stoichiometric combination of elements. Li_{4-2x}M_xⁿ⁺P₂S₆ (M = V, Fe, Ni, Co, and Zn; x = 0.5–1, n = 2 or 3) crystallize in the *P*31*m* space group, while Li₂MnP₂S₆ crystallizes in *R*3̄. All the compounds form a 2D layered structure through edge sharing MS₆ octahedra and P₂S₆ units with Li atoms occupying the interlayer spaces. X-ray diffraction and thermogravimetric analyses reveal spontaneous water intercalation tendencies of these materials, leading to two distinct hydrated phases (HY-I and HY-II) when they are exposed to air for shorter and extended times, respectively. Thermogravimetric analyses demonstrate the reversibility of phase transformation upon deintercalation of water molecules from the interlayer regions. The crystal structure of hydrated phase I from single-crystal and synchrotron powder X-ray diffraction indicates formation of a monolayer of water with interlayer expansion. Additionally, Li_{4-2x}M_xⁿ⁺P₂S₆ (M = V, Mn, Fe, and Ni) also display huge affinity toward NH₃ intercalation in the interlayer space when subjected to a liquid or gaseous ammonia environment. The magnetic measurements on Li₂MP₂S₆ (M = Mn and Ni) show the paramagnetic nature of the compounds down to 2 K. AC impedance spectroscopy on Li_{2.56}Zn_{0.72}P₂S₆ shows a room-temperature ionic conductivity of 2.69 × 10⁻³ mS/cm, which is four orders higher in magnitude than Li₄P₂S₆, while hydrated Li_{2.56}Zn_{0.72}P₂S₆ display 7-fold higher ionic conductivity (1.85 × 10⁻² mS/cm) than its anhydrous counterpart. The study also reports electrochemical Li (de)intercalation in Li₂FeP₂S₆ in a Li-ion battery with a liquid electrolyte for the first time.



INTRODUCTION

The family of two-dimensional (2D) metal thiophosphates, M₂P₂S₆ (MPS₃) (M = Mn, Fe, Co, Ni, Zn, and Cd), has been widely explored for numerous properties such as energy storage, chemical intercalation, and magnetic properties in low dimensions.^{1–11} The synthesis and crystal structures are extensively studied by Hahn et al., Klingens et al., and Rouxel et al. where they found that the layers are formed by the edge-sharing MS₆ and P₂S₆ polyhedral units and held together by van der Waals (vdW) forces.^{12–14} For several years, this van der Waals gap in M₂P₂S₆ was utilized for intercalating various host ions to tune the properties of 2D materials targeting specific applications.^{2–4,15,16} During this intercalation process in an aqueous medium, Clement discovered that hydrated inorganic and some small organometallic cations intercalate in the van der Waals gap where the charge of the guest is compensated by leaching out intralayer metal ions as in M_{1-x}PS₃G_{2x}(H₂O)_y (G is a guest species of +1 charge).¹⁷ This intercalation was unusual as it did not involve electron transfer

as in a reductive insertion but occurred through cation migration from a solid to the solvent.¹⁸ Due to the incorporation of a hydration shell around the intercalant, there is a huge expansion of interlayer spacings, and the subsequent effect of that on properties became an interesting area of research. For example, the partly proton-exchanged phase of Li-intercalated CdPS₃, Cd_{0.85}PS₃Li_{0.15}H_{0.15}, displayed excellent proton ion conduction.¹⁹ The crystal structure of this hydrated intercalated phase is still unsettled, except in few cases where it showed transition from a monoclinic to more symmetric hexagonal crystal system.²⁰ Recently, Feng et al.

Received: November 4, 2023

Revised: March 24, 2024

Accepted: March 25, 2024

Published: April 5, 2024



reported the co-intercalation of NH_3 and alkali metals into FePS_3 layers employing a liquid ammonia method, where charge compensation is achieved through charge transfer from an alkali metal to an FePS_3 unit in compositions $\text{A}(\text{NH}_3)_x\text{FePS}_3$ ($\text{A} = \text{Li}$ and K).²¹ Taking cue from these hydrated or solvated alkali ion-intercalated phases, a new family of materials can be envisioned from the $\text{M}_2\text{P}_2\text{S}_6$ structure through replacement of part of the divalent transition metal with alkali metals, giving rise to a composition, $\text{A}_{2x}\text{M}_{2-x}\text{P}_2\text{S}_6$ ($\text{A} =$ alkali ions, $\text{M} =$ divalent metals, and $x =$ between 0 and 1). The derived crystal structures will be similar to the ion exchange-intercalated phases of $\text{M}_2\text{P}_2\text{S}_6$ but differ in the occupancy of transition metal sites. For example, in $\text{Li}_2\text{MP}_2\text{S}_6$, alkali ions occupy the van der Waals gap and half of the transition metal sites, while the ion exchange compounds have an equivalent number of vacancies in the transition metal sites to balance the charge of intercalated ions, leading to metal-deficient phases. $\text{Li}_2\text{MP}_2\text{S}_6$ phases can also be thought of being derived from $\text{Li}_4\text{P}_2\text{S}_6$ by partially replacing Li ions by a divalent metal. This also brings opportunities to employ a solid-state metathesis route in which a P_2S_6 building unit containing a precursor, $\text{Li}_4\text{P}_2\text{S}_6$, can be reacted with metal chlorides to rationally synthesize $\text{Li}_2\text{MP}_2\text{S}_6$ in a so-called building-block approach.^{22,23} In this approach, we hypothesize that the alkali metal-containing molecular building unit ($\text{P}_2\text{S}_6^{4-}$) during reaction with metal halides will remain intact to produce the desired product ($\text{Li}_{4-2x}\text{M}_x\text{P}_2\text{S}_6$) rationally through the partial replacement of alkali ions by the metal of the metal halide precursor, eliminating the possibility of formation of multiple products.

If the metal of choice is a transition metal, then the resulting $\text{Li}_{4-2x}\text{M}_x\text{P}_2\text{S}_6$ (where M is a +2 metal ion) can be a potential candidate for the cathode. On the other hand, if it is a redox-inactive metal, then they could be a candidate for solid electrolytes as an equivalent number of vacancies can be created in $\text{Li}_4\text{P}_2\text{S}_6$ by the replacement of two monovalent Li^+ for every divalent M^{2+} . Takada et al. first reported the synthesis of $\text{Li}_{4-2x}\text{M}_x\text{P}_2\text{S}_6$ ($\text{M} = \text{Mg}$ and Fe) under anhydrous conditions in a sealed quartz tube and determined its crystal structure in the trigonal system ($\text{P}\bar{3}1m$).^{24,25} Accordingly, $\text{Li}_2\text{MgP}_2\text{S}_6$ displayed couple of orders higher Li-ion conductivity compared to pure $\text{Li}_4\text{P}_2\text{S}_6$, whose room-temperature conductivity is found to be 1.6×10^{-7} S/cm,²⁴ while on the other hand, $\text{Li}_2\text{FeP}_2\text{S}_6$ is a 3 V cathode.²⁵ Lotsch's group showed that partial substitution of M^{3+} in $\text{Li}_4\text{P}_2\text{S}_6$ can also stabilize the trigonal $\text{Li}_{4-2x}\text{M}_x\text{P}_2\text{S}_6$ structure type as in the case of $\text{Li}_{4-3x}\text{Sc}_x\text{P}_2\text{S}_6$ ($x = 0.358$).²⁶ More recently, Rodriguez's group further expanded the family of $\text{Li}_2\text{MP}_2\text{S}_6$ structure type with new compositions of Fe and Co and reported their magnetic properties.²⁷ Interestingly, they claimed that in $\text{Li}_{1.56}\text{Co}_{0.71}\text{P}_2\text{S}_6$, P_2S_6 is redox non-innocent in nature and carries a -3 charge instead of -4 . Considering the vast structural and compositional flexibility, the ability to accommodate various host ions in the interlayer gap, and generation of exotic magnetic properties as exemplified by the vacancy-containing $\text{M}_{1-x}\text{PS}_3\text{G}_{2xy}(\text{H}_2\text{O})_y$ systems with different transition metals, the $\text{Li}_{4-2x}\text{M}_x\text{P}_2\text{S}_6$ family of compounds can be considered as an important structure type that is still at its infancy. Further works on this class of materials is much sought after to answer questions related to solvent intercalation, non-innocence nature of the P_2S_6 unit, and structural uniformity across the first transition series to further broaden the scope of applications.

In this work, we are reporting both the metathesis building-block approach and stoichiometric routes of synthesis of $\text{Li}_{4-2x}\text{M}_x\text{P}_2\text{S}_6$ ($\text{M} = \text{V}$, Mn , Fe , Co , Ni , and Zn ; $x = 0.5-1$, $n = 2$ or 3) and showcasing various intercalation properties by this family of non-vdW 2D compounds. Reversible intercalation of atmospheric water and intake of ammonia molecules from liquid and gaseous ammonia are demonstrated. The ionic conductivity of anhydrous and hydrated $\text{Li}_{2.56}\text{Zn}_{0.72}\text{P}_2\text{S}_6$ shows approximately four and five orders higher Li-ion conduction, respectively, over $\text{Li}_4\text{P}_2\text{S}_6$. Magnetic properties of $\text{Li}_2\text{MP}_2\text{S}_6$ ($\text{M} = \text{Mn}$ and Ni) are studied for the first time. Finally, we also report the electrochemical activity of $\text{Li}_2\text{FeP}_2\text{S}_6$ with a liquid electrolyte in a Li-ion battery for the first time.

EXPERIMENTAL SECTION

Synthesis. Compounds with a targeted nominal composition of $\text{Li}_2\text{MP}_2\text{S}_6$ ($\text{M} = \text{V}$ (1), Mn (2), Fe (3), Co (4), Ni (5), and Zn (6)) were synthesized by two different routes: (i) from stoichiometric metathetic reaction of the preformed Li-containing P_2S_6 building block, $\text{Li}_4\text{P}_2\text{S}_6$, with metal chloride (MCl_2 , where $\text{M} = \text{Mn}$, Fe , Co , Ni , and Zn ; VCl_3) and (ii) by taking stoichiometric ratios of binaries and metallic elements. For the metathesis reactions, first, $\text{Li}_4\text{P}_2\text{S}_6$ was synthesized following a reported procedure²⁸ and reacted with MCl_x ($\text{M} = \text{V}^{3+}$, Fe^{2+} , Mn^{2+} , Fe^{2+} , Co^{2+} , Ni^{2+} , and Zn^{2+} ; 99.99%, Alfa Aesar) in equimolar ratio at 1 mM scale. For the second method, the solid-state reactions were carried out with 1 mM Li_2S (99.98%, Sigma-Aldrich), 1 mM metallic M powder (99.9%, Sigma-Aldrich), and 1 mM P_2S_5 (Sigma-Aldrich) in vacuum-sealed quartz ampules. The precursors were loaded in a carbon-coated quartz ampule inside an argon-filled glovebox ($\text{O}_2 < 0.5$ ppm and $\text{H}_2\text{O} < 0.5$ ppm). The ampules were taken out of the glovebox with airtight adaptors to avoid any exposure to the air and were flame-sealed under vacuum. The ampule with an inner diameter of 10 mm and an outer diameter of 12 mm had a length of ~ 130 mm after sealing. In the case of metathesis reactions, the ampules were heated at a ramp of 35 °C/h to 650 °C and held at that temperature for 24 h, followed by cooling to room temperature at 35 °C/h rate. For the nonmetathetic stoichiometric reactions, the sealed ampules were heated in a temperature-controlled furnace at a ramping rate of 40 °C/h to 700 °C and dwelled at that temperature for 15 h before cooling it to room temperature at 40 °C/h. The cooled ampules were taken inside the glovebox, and samples were recovered. Dark brown-colored compounds for V (1), Fe (3), Co (4), and Ni (5) while slightly off white samples for Mn (2) and Zn (6) were recovered from the reacted ampules. A digital picture of the powder samples obtained from nonmetathetic stoichiometric reactions is given in Figure S1, and similar colored samples were also obtained from metathesis reactions. When exposed to air, all samples quickly absorb moisture and exfoliate within a matter of few minutes. V (1) and Zn (6) tend to hydrolyze if left for an extended time. However, the samples do not seem to be particularly sensitive to oxygen. Hence, handling of samples requires great care to measure the property of anhydrous samples. Crystals were picked by visual inspection under an optical polarizing microscope from compounds 1, 2, and 4 for single-crystal X-ray diffraction from nonmetathetic reactions, and all the samples were finely ground using an agate mortar and pestle to collect the powder X-ray diffraction data. For the ammonia intercalation reaction, 200 mg of compounds of 1 (V), 2 (Mn), 3 (Fe), and 5 (Ni) was preheated at 200 °C for 4 h under vacuum and liquid ammonia was condensed on the sample taken in a sublimator. The details of the ammonia intercalation reaction from liquid ammonia are given in the Supporting Information. The PXRD of the ammonia-intercalated samples was collected in an airtight cell, and TG-DSC was performed by quickly transferring the sample in the DSC cup.

Physical Methods. Synthesized compounds were analyzed on elemental content using the ICP method and investigated by spectroscopic (IR and UV-vis spectroscopy as diffused reflectance)

methods, X-ray analysis (both single-crystal and powder diffraction, including variable temperature), thermal analysis, scanning electron microscopy, ionic conductivity, and electrochemical and magnetic measurements. Further experimental details are presented in the [Supporting Information](#) of this paper.

Single-Crystal X-ray diffraction. The crystal structures of **1** (V), **2** (Mn), **4** (Co), and the hydrated phase of **2** (**2-HY-I**) were solved from single-crystal intensity data sets. Further details of data collections are given in the [Supporting Information](#). Both **1** and **4** crystallized in the $P\bar{3}1m$ space group as previously reported for this class of layered materials with honeycomb ordering in the layers. All the atoms in the crystal structures were located from the difference Fourier maps, and the weighted R factor, wR_2 , converged to a low value with no further residual electron densities. In both compounds, we found a mixed occupancy of Li/M ($M = V$ and Co) in the M site (Wyckoff site, $2d$). Disorder in the phosphorus site was observed only in compound **1**, with a small percentage of P being present in the Li layer. These results (P-disorder) are slightly different from those reported by Takada et al. for Fe²⁵ but similar to those reported by Takada et al. for Mg in $Li_{4-2x}Mg_xP_2S_6$ and by Diethrich et al. for Co (discussed later).^{24,27} Based on the occupancy refinements of Li/M, we arrived at the final compositions of $Li_{2.5}V_{0.5}P_2S_6$ (**1**) and $Li_{2.5}Co_{0.75}P_2S_6$ (**4**), assigning oxidation states of V and Co as +3 and +2, respectively. Compound **2** crystallized in the rhombohedral space group of $R\bar{3}$ in trigonal cell setting. Unlike other structures, we found that Mn atoms were present in two distinct Oh sites. The mixed occupancy of Mn1/Li1 (65%/35%) can be refined in the $3a$ Wyckoff site, while in the $6c$ Wyckoff site, 50% of the site is occupied by Mn2/Li2 (17.5%/32.5%) and the remaining 50% by the P_2 dimer. The hydrated phase of compound **2** (**2-HY-I**), on the other hand, crystallized in the $C2/m$ space group, where Mn1/Li1 occupies the $4h$ Wyckoff site with a minor component of P_2 dimer, while the Oh site ($4i$) is occupied by the P_2 dimer with a minor percentage of Mn/Li. From the Fourier map, we could locate the oxygen atoms bonded to the interlayer Li site. It should be noted here that the crystals of these compounds are very thin plates, and it is extremely difficult to find a single crystal that does not have any stacking fault or twinning. The crystal structure solutions of **2** and **2-HY-I** may have artifacts from their approximate treatments as single domain crystals (including high R_1 and R_{int} values, large difference map peaks, and anomalous thermal displacement parameters). The differences in the percentages of disordered atoms in the Oh site are also a consequence of single-domain treatment. However, the agreement between measured powder diffraction and simulated patterns from single-crystal coordinates (discussed below) indicates that the unit cells and crystal systems are likely correct, and our crystal structure at least qualitatively distinguishes between full and partly occupied metal atom sites. The crystal structure data and the refinement parameters are provided in [Table 1](#) (for compounds **1** and **4**) and [Table S1](#) (for **2** and **2-HY-I**). The selected bond lengths are given in [Tables 2](#) and [3](#). The atomic coordinates of **1**, **2**, **4**, and **2-HY-I** from single-crystal structure solutions are given in [Table S2](#) and can also be obtained from CCDC by quoting the following numbers: 2331996 (**1**), 2331707 (**2**), 2331997 (**4**), and 2331708 (**2-HY-I**).

Powder X-ray Diffraction. The laboratory powder data of samples obtained from the metathesis and stoichiometric elemental route matched well with the simulated pattern of $Li_2MP_2S_6$ ²⁵ ([Figure 1a,b](#)), except for the $CoCl_2$ reaction in the metathesis route. The reaction between $Li_2P_2S_6 + CoCl_2$ did not produce the intended product, $Li_2CoP_2S_6$; instead, it produced some unknown phase ([Figure S2](#)).

However, we also noticed an extra line around $Q = 0.7 \text{ \AA}^{-1}$ ($d = 8.97 \text{ \AA}$) appearing consistently in all the compounds, which was not from the as-synthesized phase. The low Q -space peak (at 0.7 \AA^{-1}) has been attributed to the intercalation of water in the interlamellar space by part of the sample as confirmed by the thermodiffraction, IR, and TGA studies (discussed later). The sensitivity of this class of alkali metal-intercalated 2D materials to absorb the atmospheric moisture is not unusual as it has been observed previously in several cases.^{29–32} In addition, we collected high-resolution synchrotron

Table 1. Crystal Structure Data and Refinement Parameters for $Li_{2.5}V_{0.5}P_2S_6$ (1**) and $Li_{2.5}Co_{0.75}P_2S_6$ (**4**)**

compound	1	4
empirical formula	$Li_{2.5}V_{0.5}P_2S_6$	$Li_{2.5}Co_{0.75}P_2S_6$
formula weight	296.99	315.85
temperature	223(2) K	250(2) K
wavelength	0.71073 Å	0.71073 Å
crystal system	trigonal	trigonal
space group	$P\bar{3}1m$	$P\bar{3}1m$
$a/\text{Å}$	6.010(2)	5.9950(6)
$b/\text{Å}$	6.010(2)	5.9950(6)
$c/\text{Å}$	6.537(3)	6.5206(7)
volume/Å ³	204.46(18)	202.95(5)
Z	1	1
density (calculated)	2.412 Mg/m ³	2.584 Mg/m ³
absorption coefficient	2.502 mm ⁻¹	3.461 mm ⁻¹
goodness of fit on F^2	1.324	1.260
$R [I > 2\sigma(I)]^a$	$R_1 = 0.0300$	$R_1 = 0.0312$
$wR (F^2)$ (all data) ^b	$wR_2 = 0.0756$	$wR_2 = 0.0890$
$R(\text{int})$	0.0506	0.0280
$\delta F/e \text{ \AA}^{-3}$	1.15 and -1.21	1.65 and -0.42

^a $R_1 = \sum ||F_o| - |F_c|| / \sum |F_o|$. ^b $wR_2 = \{ \sum [w(F_o^2 - F_c^2)]^2 / \sum [w(F_o^2)]^2 \}^{1/2}$, where $w = 1 / [\sigma^2(F_o^2) + (aP)^2 + bP]$, where $P = (F_o^2 + 2F_c^2) / 3$.

Table 2. Selected Bond Lengths for $Li_{2.5}V_{0.5}P_2S_6$ (1**), $Li_{2.5}Co_{0.75}P_2S_6$ (**4**), and $Li_{2.4}Ni_{0.8}P_2S_6$ (**5**)**

M–S	M = V	M = Co	M = Ni
M1–S1	2.577(9)	2.5649(5)	2.5575(9)
P1–S1	2.025(3)	2.0208(7)	2.0257(3)
P1A–S1	2.031(9)		
Li2–S1	2.625(3)	2.6219(5)	2.6297(5)

Table 3. Selected Bond Lengths for $Li_2MnP_2S_6$ (2**)**

M–S	M = Mn
M1–S1	2.640(3)
M2–S1	2.637(9)
M2–S1 ^a	2.515(9)
P1–S1	2.069(4)
P2–S1	2.061(4)

^a $-x + 4/3, -y + 5/3, -z + 2/3$.

powder X-ray diffraction (S-PXRD) data from APS (Argonne National Laboratory) for **2** (Mn), **5** (Ni), and the hydrated phase of **2** (**2-HY-I**) to refine the data using the single-crystal coordinates of **2** (Mn), Fe,²⁵ and **2-HY-I**, respectively. The anhydrous phases of compounds **2** (Mn) and **5** (Ni) were generated by heating the samples at 200 °C for 6 h under vacuum and sealed in a quartz capillary for data collection. The Rietveld refinement using GSAS-II³³ though had a signature of highly preferred orientation in the difference curve as given in [Figure 2](#) for **2** and **5** and in [Figure S3](#) for **2-HY-I**, however, the refinements converged to reasonably low values of R_w after refining the unit cell, atomic coordinates, and isothermal displacement parameters as given in [Table 4](#) (for **2** and **5**) and in [Table S3](#) (for **2-HY-I**). The refined unit cell parameters and bond length distributions of each atom were similar to our single-crystal structure solution. It is to be noted here that similar to single-crystal data, the S-PXRD of **2** (Mn) could not be indexed in the normal trigonal and convergence was much better in the tripled c -axis in the rhombohedral $R\bar{3}$ space group. In the case of **5** (Ni), we refined our data using the $Li_2FeP_2S_6$ crystal structure as our initial structure model as the S-PXRD indexed in the trigonal cell similar to $M = V$, Fe, and Co. Through the refinement, we also found a slightly different Ni/Li ratio (40:60) in the $2d$ site that deviated from the nominal

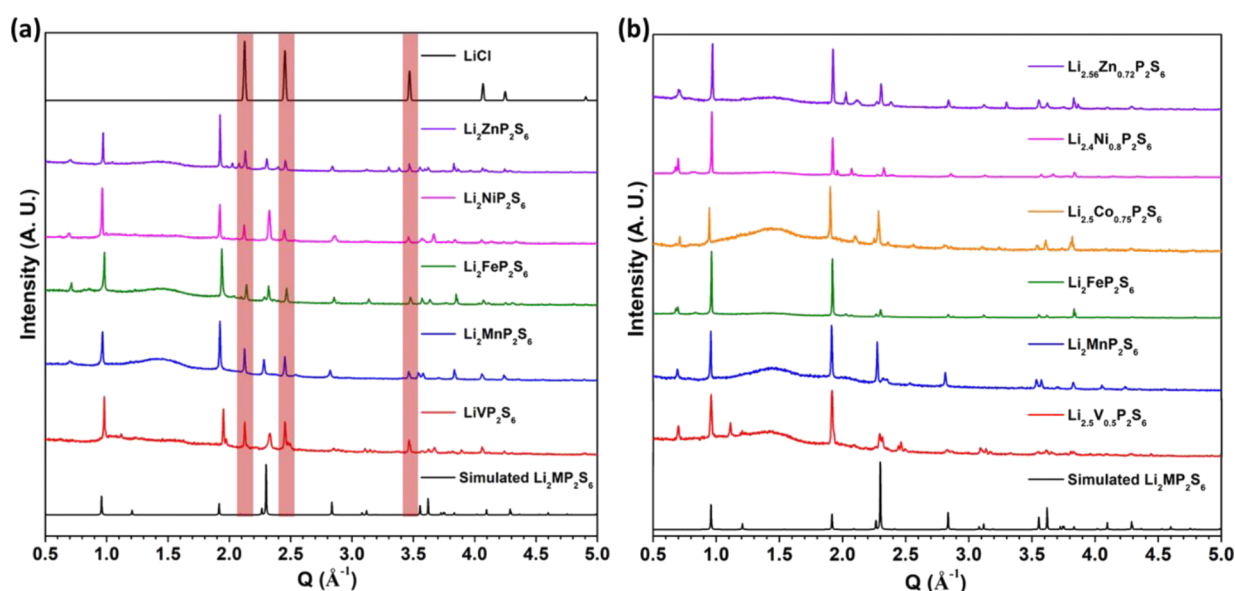


Figure 1. Laboratory powder X-ray diffraction and simulated pattern of $\text{Li}_2\text{MP}_2\text{S}_6$. The small peak near $Q = 0.7 \text{ \AA}^{-1}$ indicates partial transformation to the hydrated phase.

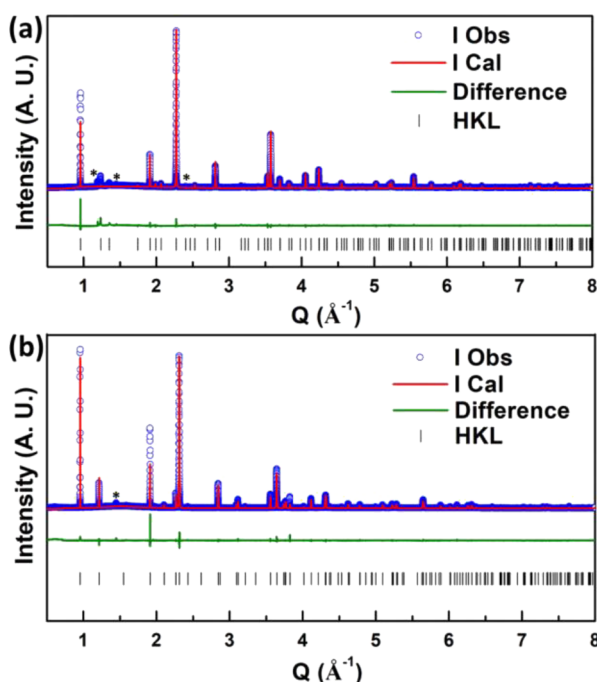


Figure 2. Rietveld refinement on the synchrotron PXRD pattern of anhydrous (a) $\text{Li}_2\text{MnP}_2\text{S}_6$ (2) and (b) $\text{Li}_{2.4}\text{Ni}_{0.8}\text{P}_2\text{S}_6$ (5). Impurity lines are marked with asterisks.

composition of 50:50 and led to the composition of $\text{Li}_{2.4}\text{Ni}_{0.8}\text{P}_2\text{S}_6$ (5). However, both the samples (2 and 5) had minor unknown impurity lines, which were disregarded during the refinements. The readers should also be alerted that 00 l lines for 5 did not fit well. They are much sharper than other lines due to diffraction domains preferentially oriented along the c -axis. We did not get single crystals or perform any refinement of structural data for compounds with $M = \text{Fe}$ and Zn , and their identity and phase purity have been verified by laboratory PXRD (Figure 1) and thermodiffraction (discussed later). The compositions of compounds with $M = \text{Fe}$ and Zn are assigned as $\text{Li}_2\text{FeP}_2\text{S}_6$ and $\text{Li}_{2.56}\text{Zn}_{0.72}\text{P}_2\text{S}_6$, respectively, based on the Li/M ratio obtained from ICP-OES analysis. All the subsequent

Table 4. Refined Lattice Constants and Final Rietveld Refinement of $\text{Li}_2\text{MnP}_2\text{S}_6$ (2) and $\text{Li}_{2.4}\text{Ni}_{0.8}\text{P}_2\text{S}_6$ (5)

compound	2	5
empirical formula	$\text{Li}_2\text{MnP}_2\text{S}_6$	$\text{Li}_{2.4}\text{Ni}_{0.8}\text{P}_2\text{S}_6$
formula weight	323.12	317.93
crystal system	rhombohedral	trigonal
space group	$R\bar{3}$	$P\bar{3}1m$
$a/\text{\AA}$	6.090(2)	5.975(6)
$b/\text{\AA}$	6.090(2)	5.975(6)
$c/\text{\AA}$	19.712(3)	6.573(7)
volume/ \AA^3	633.213(8)	203.298(5)
Z	2	1
density (calculated)	2.542 Mg/m^3	2.597 Mg/m^3
R_w (%)	0.1490	0.0939

property studies are done with the products of nonmetathesis stoichiometric synthesis as they are well characterized.

ICP-OES. To clear the uncertainty in the Li concentration and verify the compositions of each compound, we performed ICP-OES analysis on a manually separated milligram amount of plate-shaped crystals of each sample from the stoichiometric elemental reaction products. The results of Li/M ratios of each compound from the analysis are in good agreement with our expected values from a single crystal and the refined composition from S-PXRD (Table S4). However, they do deviate from the nominal composition except for 2 (Mn) and 3 (Fe). It is thus safe to assign the following compositions for the compounds, $\text{Li}_{2.5}\text{V}_{0.5}\text{P}_2\text{S}_6$ (1) and $\text{Li}_{4-2x}\text{M}_x\text{P}_2\text{S}_6$, where $x = 1$ for Mn (2) and Fe (3), 0.75 for Co (4), 0.8 for Ni (5), and 0.72 for Zn (6).

Magnetic Measurements. The magnetic properties of Co and Fe with compositions $\text{Li}_{1.56}\text{Co}_{0.71}\text{P}_2\text{S}_6$ and $\text{Li}_{2.26}\text{Fe}_{0.94}\text{P}_2\text{S}_6$ have been reported recently by Diethrich et al.²⁷ Herein, we report preliminary magnetic properties of 2 and 5, mainly as a characterization tool to confirm the oxidation state of Mn and Ni and to evaluate if there is any magnetic transition. The temperature-dependent molar magnetic susceptibility (χ_M) and inverse molar susceptibility ($1/\chi_M$) of compounds 2 and 5 are shown in Figure 3a,b. With lowering temperature from 300 to 2 K, the molar magnetic susceptibility increases asymptotically and reaches maxima of 0.287 and 0.200 emu mol^{-1} for compounds 2 and 5, respectively, at 2 K. Further, no divergence is observed in the FC and ZFC susceptibility, indicating no magnetic ordering, and the compounds are paramagnetic in nature

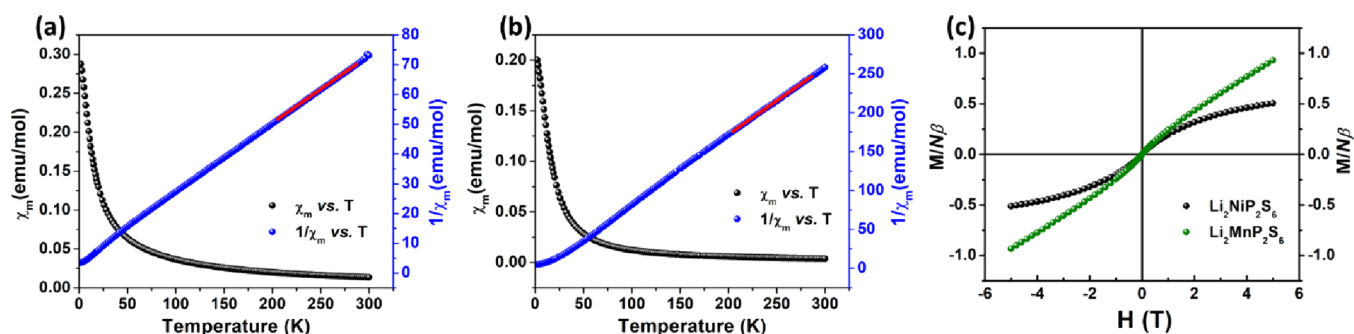


Figure 3. Temperature-dependent molar magnetic susceptibility and inverse molar magnetic susceptibility plots at an applied magnetic field of 1 T: (a) $\text{Li}_2\text{MnP}_2\text{S}_6$ (2) and (b) $\text{Li}_{2.4}\text{Ni}_{0.8}\text{P}_2\text{S}_6$ (5). (c) Field-dependent magnetization at 5 K for both compounds.

between 300 and 2 K. The $1/\chi_M$ vs T shows a linear region between 300 and 25 K, and at lower temperatures, the curve deviates from the linearity. From the linear fit of the curve at higher temperatures with Curie–Weiss law $1/\chi_M = C/(T - \theta_p)$, Weiss (θ_p) and Curie constant (C) are obtained. From the Curie constant, the paramagnetic moment is calculated and compared with the theoretical spin-only moments of Mn^{2+} and Ni^{2+} ions. The experimental magnetic moments of 5.90 and $3.04 \mu_B$ for Mn and Ni, respectively, calculated from $\mu_{\text{exp}} = \sqrt{8C}$ are very close to the theoretically calculated values of 5.91 and $2.82 \mu_B$, respectively, confirming the +2 oxidation state of these transition metals and also indirectly confirming the compositions. The small negative values of the Weiss constant θ_p , -15.64 and -0.335 , for 2 and 5, respectively, indicate the presence of some antiferromagnetic correlations in the paramagnetic region, which could not lead to any AF ordering above 2 K. The isothermal magnetization (M) measured at 5 K for both samples shows a sluggish increase in magnetization and does not show any significant hysteresis while reversing the field (Figure 3c). However, in the case of 5, we did observe a very small hysteresis, with a negligible remanent magnetization of $0.003N\beta$ (within the measurement uncertainty) and a coercive field of ~ 11.2 Oe (Figure S4). The S-shaped nature and weak hysteresis may indicate the presence of ferro/ferromagnetic interactions at low temperatures, which could not lead to long-range ferromagnetic ordering until 2 K. The maximum magnetization values of 0.931 and $0.506 N\beta$ for 2 and 5, respectively, reached at 5 T are only 18.6 and 25.3% of their theoretical saturation moment ($M_s = gSN\beta$), assuming complete attainment of parallel spins.

Optical Band Gap Studies. DRS measurements were performed on each sample to estimate the optical band gap of the compounds. The $(\alpha h\nu)^2$ vs $h\nu$ (eV) plot shows a flat line with few small jumps in the lower energy scale corresponding to weak $d-d$ transition followed by a steep rise due to the electronic transition from the valence band to the conduction band (Figure S5). The band gap was determined by the extrapolation of base flat line and the steep rise of the curves. The band gap of the compounds ranges from 1.5 to 3.65 eV (Table S5), indicating a wide range of band gaps particularly useful for optoelectronic applications. It is to be noted here that band gaps of Li-inserted samples are close to the band gap of corresponding $\text{M}_2\text{P}_2\text{S}_6$ phases.^{2,34}

RESULTS AND DISCUSSION

Structural Description. Compounds $\text{Li}_{4-3x}\text{V}_x\text{P}_2\text{S}_6$ ($x = 0.5$) (1), $\text{Li}_{4-2x}\text{Co}_x\text{P}_2\text{S}_6$ ($x = 0.75$) (4), and $\text{Li}_{4-2x}\text{Ni}_x\text{P}_2\text{S}_6$ ($x = 0.8$) (5) crystallize in the $\overline{P}31m$ space group isostructural to $\text{Li}_{4-3x}\text{Sc}_x\text{P}_2\text{S}_6$ ²⁶ or $\text{Li}_{4-2x}\text{M}_x\text{P}_2\text{S}_6$ ($M = \text{Mg, Fe, and Co}$).^{24,25,27} The asymmetric unit of the crystal structures of 1, 4, and 5 consists of one transition metal (V, Co, or Ni) mixed-occupied with Li (Li1), one disordered phosphorus split between P1 (major component) and P1A (minor component) for 1 (no disorder in P for 4 and 5), one sulfur, and one lithium site (Figure 4a,b). In both cases, 2D layers are formed in the ab -

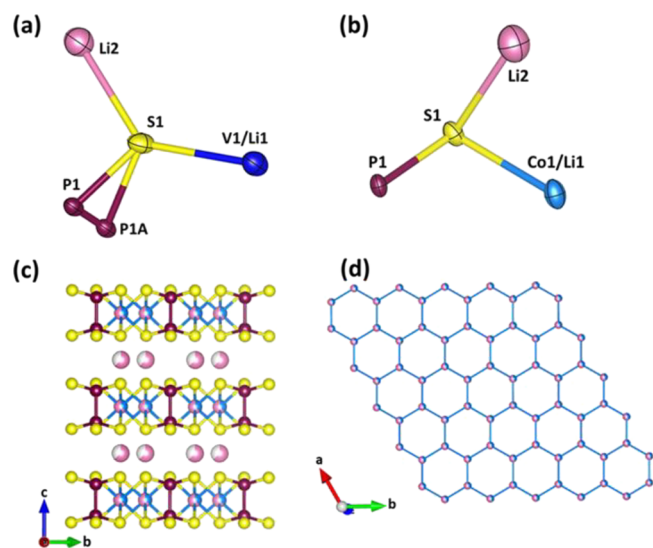


Figure 4. (a) Asymmetric unit of $\text{Li}_{2.5}\text{V}_{0.5}\text{P}_2\text{S}_6$ with thermal ellipsoids given at 50% probability. (b) Asymmetric unit of $\text{Li}_{2.5}\text{Co}_{0.75}\text{P}_2\text{S}_6$ with thermal ellipsoids given at 50% probability. (c) 2D layer formed through the connectivity of P_2S_6 and MS_6 polyhedral units along the c -axis with Li in the interlayers. (d) Honeycomb ordering of transition metal sites in the ab -plane of the layers.

plane by edge sharing between MS_6 octahedra themselves or between MS_6 octahedra and P_2S_6 polyhedra and stacked along the c -axis with Li ions filling the interlayer van der Waals gap (Figure 4c). Both structures form ordered honeycomb layers connecting the transition metal sites in the ab -plane (Figure 4d).

Such honeycomb layers are stacked exactly on top of each other along the c -axis with partially occupied Li atoms sandwiched between two such anionic honeycomb layers. The P–P dimer resides exactly in the middle of hexagon with the P–P bond perpendicularly disposed to the honeycomb layers. The crystal structures can also be described in terms of packing of anions. The S atoms form hexagonal close-packing arrangements, and they are stacked in ABAB fashion along the c -axis. Such stacking creates 6 octahedral (Oh) holes and 12 tetrahedral (Td) holes if the formula is written as $\text{Li}_x(\text{M}_{2-x}\text{Li}_x)\text{P}_2\text{S}_6$. Here, all the Td holes are empty and only 2/3rd of the Oh holes are filled when $x = 1$. The manner in which the Oh holes are filled makes this compound different from $\text{M}_2\text{P}_2\text{S}_6$ and $\text{Mn}_{2-x}\text{PS}_3\text{G}_{2x}(\text{H}_2\text{O})_y$.^{1,17,18} The P_2 dimer and mixed M/Li together fill 1/2 of the Oh holes between two hcp layers, which alternate with cation layers in which only 1/6th of the Oh holes are filled by Li. When M is a +3 cation,

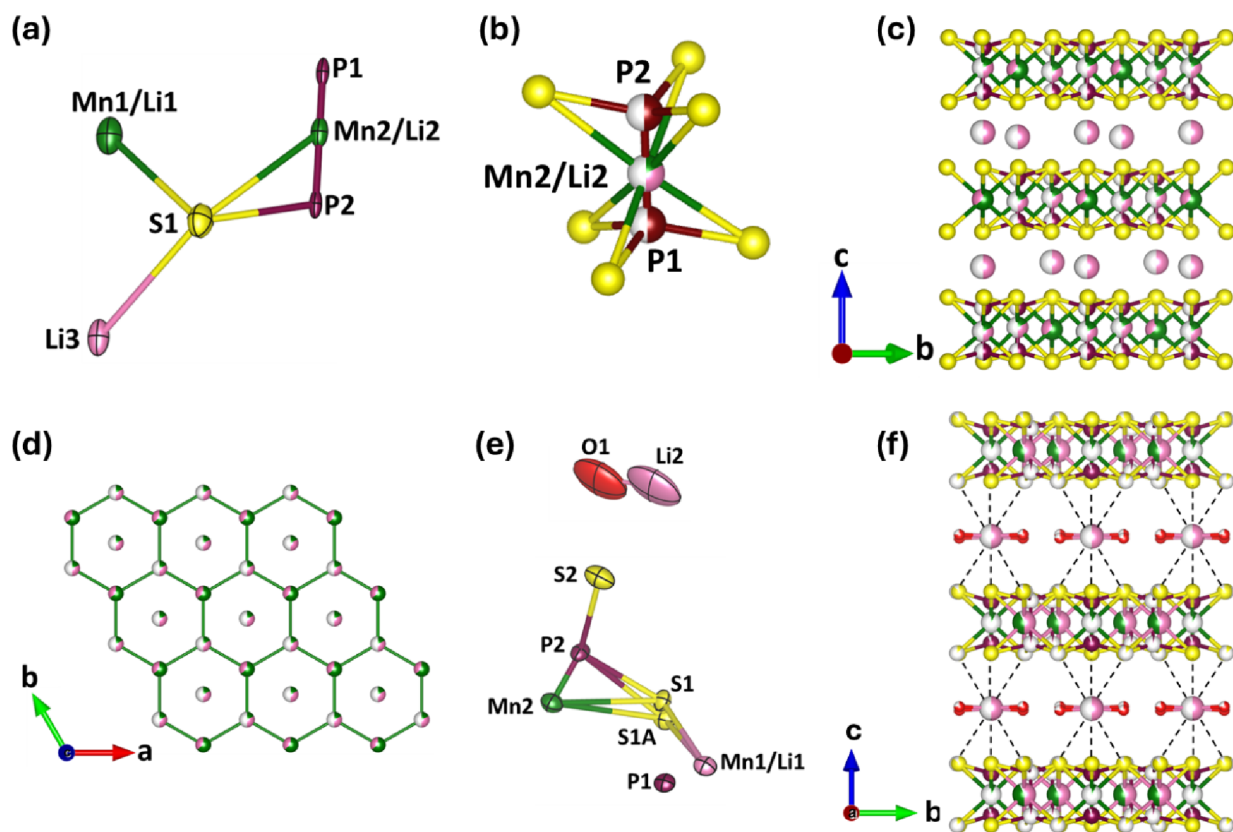


Figure 5. (a) Asymmetric unit of $\text{Li}_2\text{MnP}_2\text{S}_6$ (**2**). (b) Disordered phosphorus and manganese site in the Oh hole. (c) 2D layer formed through joining of P_2S_6 and MnS_6 polyhedral units along the c -axis with Li in the interlayers. (d) Honeycomb ordering of transition metal sites in the bc -plane of the layers with the Mn2/Li2 site at the center of each honeycomb. (e) Asymmetric unit of $\text{Li}_2\text{MnP}_2\text{S}_6 \cdot 2.48\text{H}_2\text{O}$ (**2-HY-I**). (f) 2D layer with expansion along the c -axis and Li in the interlayers with intercalated water.

then Li occupancy in the pure Li layer (Oh layer) is only 1/12th as in the case of **1**. Since we have disorder in the P site in **1**, this means that a minor component (4.4%) of the P–P dimer takes up Oh holes in the pure Li layers and the same amount of P_2 vacancy created in the $(\text{V}_{2-x}\text{Li}_x)\text{P}_2$ layer. A similar P_2 distribution has been reported in the case of $\text{Li}_{4-2x}\text{Mg}_x\text{P}_2\text{S}_6$ and $\text{Li}_{1.56}\text{Co}_{0.71}\text{P}_2\text{S}_6$.^{24,27} However, in contrast to $\text{Li}_{1.56}\text{Co}_{0.71}\text{P}_2\text{S}_6$ reported by Diethrich et al.,²⁷ our crystal structure solution of compound $\text{Li}_{4-2x}\text{Co}_x\text{P}_2\text{S}_6$ ($x = 0.75$) (**4**) differs significantly. In our solution, we have modeled the 2c site as jointly occupied by Co and Li, holding their sum of occupancy as 100%, while Diethrich et al. refined the transition metal site with vacancies without introducing any Li in that site and, to balance the charge, they concluded that the P_2S_6 unit carries -3 charge instead of -4 . Therefore, the P_2S_6 unit is redox non-innocent. In our modeling, $\text{Li}_{2.5}\text{Co}_{0.75}\text{P}_2\text{S}_6$ is charge-balanced with Co in the 2+ oxidation state and the charge of the [P–P] dimer is nominally +8 (Figure 4c). We have relied more on ICP-OES measurements to correlate our Li/M ratio. Compound **2**, on the other hand, crystallizes in the $R\bar{3}$ space group, and the asymmetric unit consists of two Mn sites jointly occupied with Li (Mn1/Li1 and Mn2/Li2), one phosphorus dimer site (P_2), three sulfur, and one lithium site (Figure 5a). The Mn2/Li2 in this case shares the same octahedral site as P_2 (Figure 5b), where the center of the P–P dimer resides in the Oh hole. Further, the structure forms similar 2D layers through edge sharing of MnS_6 and P_2S_6 units and is stacked along the c -axis. The interlayer gaps thus created are occupied by the Li atoms (Figure 5c). Also, by connecting the Mn2/Li2 sites in

the layers, one could form a honeycomb lattice and the Mn1/Li1 site can be located at the center of each honeycomb formed (Figure 5d). As a consequence of these differences in the layer topology, the crystal structure of Mn (**2**) is slightly different and crystallizes with the tripled c -axis. The hydrated compound of **2** crystallizes in the $\text{C2}/m$ space group. The crystal system is isostructural to previously reported $\text{Li}_2\text{NiP}_2\text{S}_6$ ³⁵ and NH_3 -intercalated $\text{Li}(\text{NH}_3)_x\text{FePS}_3$.²¹ The asymmetric unit consists of one Mn1/Li1 mixed occupancy site, two sulfur (one disordered), two phosphorus, one oxygen, and one pure lithium site (Figure 5e). The hydrated phase also has the disorder of the Mn/Li/P atom in the Oh site in the layers with the minor component of P_2 . The structure is similar to the anhydrous phase with 2D layers formed by edge sharing of MnS_6 and P_2S_6 units. However, we found that the Li atom in the interlayer is accompanied by oxygen atoms from the intercalated water, resulting in an elongated c -axis (Figure 5f). During such elongation due to water intercalation, the layers of the structure undergo restacking along the ab -plane accompanied by an increase in β angle (104.33) that results in crystallization in the monoclinic system.

To address the possible non-innocence nature of the P_2S_6 unit, we also performed metathesis reactions between $\text{Li}_4\text{P}_2\text{S}_6$ and $\text{MCl}_2/\text{M}'\text{Cl}_3$ ($\text{M} = \text{Mn, Fe, Co, Ni, and Zn}$; $\text{M}' = \text{V}$), which can be represented by the equations $\text{Li}_4\text{P}_2\text{S}_6 + \text{MCl}_2 = \text{Li}_2\text{MP}_2\text{S}_6 + 2\text{LiCl}$ and $\text{Li}_4\text{P}_2\text{S}_6 + \text{M}'\text{Cl}_3 = \text{LiM}'\text{P}_2\text{S}_6 + 3\text{LiCl}$, where the M'' ion replaces part of Li from $\text{Li}_4\text{P}_2\text{S}_6$, and the formation enthalpy of the byproduct, $\text{LiCl}(\text{s})$ (-409 kJ/mol),³⁶ drives the reaction toward completion as demonstrated

in the synthesis of LiMnP_2S_6 .²² In these metathesis reactions, pure phase materials are expected to form simply by exchange of ions in a topotactic manner without involving any oxidation/reduction of precursors, avoiding chances of impurity phase formation as shown in Figure 6.

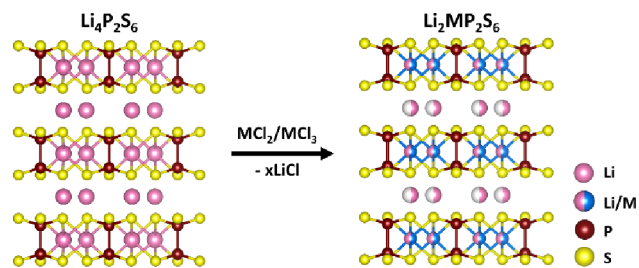


Figure 6. Building block approach leading to topotactic reaction between $\text{Li}_4\text{P}_2\text{S}_6$ and $\text{MCl}_2/\text{MCl}_3$ to form $\text{Li}_{4-nx}\text{M}_x\text{P}_2\text{S}_6$ ($n = 2$ or 3).

To our expectation, the powder diffraction patterns of metathesis route samples exactly match, except for CoCl_2 reaction with the stoichiometrically synthesized products along with lines for LiCl and a small hydration peak at lower Q -space (0.7 \AA^{-1}) (Figure 1a). However, we could not get a good size crystal to determine the single-crystal X-ray structure and refine the ratio of the M/Li site. The ICP-OES analysis could not be performed as complete removal of the byproduct LiCl from the as-synthesized product was challenging. Moreover, just single-crystal refinement from such a thin plate without ICP-based analysis may not have been enough to accurately establish the Li/M ratio. The redox non-innocence of $\text{P}_2\text{S}_6^{4-}$ will be dictated by the electron acceptability of $\text{P}_2\text{S}_6^{4-}$, which depends on the electronic band structure of $\text{P}_2\text{S}_6^{4-}$ in $\text{Li}_x\text{MP}_2\text{S}_6$. Although the electronic band structure of $\text{M}_2\text{P}_2\text{S}_6$ is still unsettled, previous reliable calculations from the tight-binding approach indicate that $\sigma_{\text{p-p}^*}$ and $\sigma_{\text{p-s}^*}$ orbitals in $\text{P}_2\text{S}_6^{4-}$ lie in too high in energy to act as a good acceptor level, which makes $\text{P}_2\text{S}_6^{4-}$ redox-inactive.^{37,38} However, accurate electronic band structure calculations of nominal $\text{Li}_2\text{MP}_2\text{S}_6$ would be required to verify the reducibility of the $\text{P}_2\text{S}_6^{4-}$ unit. In addition to that, our metathesis reaction, $\text{CoCl}_2 + \text{Li}_4\text{P}_2\text{S}_6$, also did not produce $\text{Li}_x\text{CoP}_2\text{S}_6$, which may indicate some redox or hitherto unknown reaction path. Therefore, at this point, we do not have enough evidence to conclude in favor or against the non-innocence nature of $\text{P}_2\text{S}_6^{4-}$.

Reversible Structural Transformation via Water Intercalation. As mentioned earlier, we have consistently observed a low Q -space peak ($Q = 0.7 \text{ \AA}^{-1}$) along with the expected lines for the pure phase compound in all our PXRD patterns (Figure 1). We discarded the idea of an impurity phase as we are not expecting same impurity from the metathesis reactions as well. The only other possibility for the appearance of the $Q = 0.7 \text{ \AA}^{-1}$ line might be due to interlayer expansion caused by intercalation of water molecule in a small fraction of the samples. Although samples are always handled inside a glovebox and taken out in an airtight cell, it turns out that the sample can intercalate moisture if the glovebox moisture reading rises above 2–3 ppm. A similar situation was encountered recently with Na -containing 2D gallium chalcogenides.^{29,32} Therefore, we intentionally placed our samples in air for 3 days. The powder patterns completely transformed into a fully hydrated phase with a high intense line at $Q = 0.7 \text{ \AA}^{-1}$ after 1 day and into another hydrated phase with a further

shift of the low angle line at $Q = 0.53 \text{ \AA}^{-1}$ ($d = 11.75 \text{ \AA}$) after 3 days. The 1 day and 3 day air-exposed samples are thus termed as hydrated phase-I (HY-I) and phase-II (HY-II), respectively (Figure 7). This is evident in all the samples, 1–6, indicating propensity for water intercalation with concomitant interlayer expansion by these compounds.

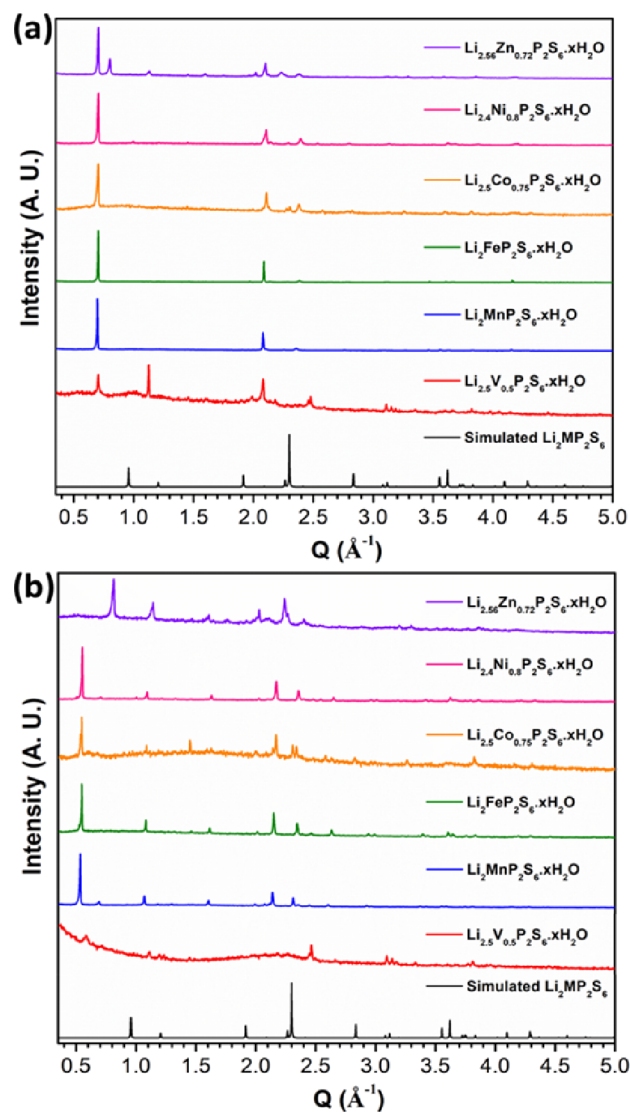


Figure 7. Laboratory powder X-ray diffraction patterns of fully hydrated $\text{Li}_2\text{MP}_2\text{S}_6$ (a) air-exposed for 1 day and (b) air-exposed for 3 days.

Fortunately, we are able to collect single-crystal X-ray diffraction data for the hydrated phase of compound 2 (Mn). The Li atom in the interlayer is bonded with two oxygen atoms of water in the Li plane and results in the expansion of lattice constant along the c -axis (Figure 5f). The Rietveld refinement of S-PXRD of the hydrated phase of 2, presumably 2-HY-I, using the single-crystal coordinates converged reasonably well with lower R_w ; however, a huge intensity mismatch is still observed due to the preferred orientations (Figure S3). Note that ordered structure coordinates were used for the refinement, ignoring the minor disordered component. The final refinement parameters are given in Table S1 along with the lattice constants, which are close to our single-crystal

structure solution. Since the PXRD of this hydrated phase displays the first line at $Q = 0.7 \text{ \AA}^{-1}$ ($d = 8.97 \text{ \AA}$), we designate this as hydrated phase-I and it has three molecules of water as water of hydration, $\text{Li}_2\text{MnP}_2\text{S}_6 \cdot 3\text{H}_2\text{O}$. To verify the reversibility of hydration–dehydration of these compounds, samples were transferred to an *in situ* heating chamber for the thermodiffraction studies. Even with minimal exposure of the samples to air while transferring into the Ar-purged heating chamber, the materials partly transform into hydrated phase-I by spontaneous intercalation of water. This is evident by room-temperature PXRD before the start of heat treatment of the sample for the thermodiffraction as shown in Figure 8 for 2-

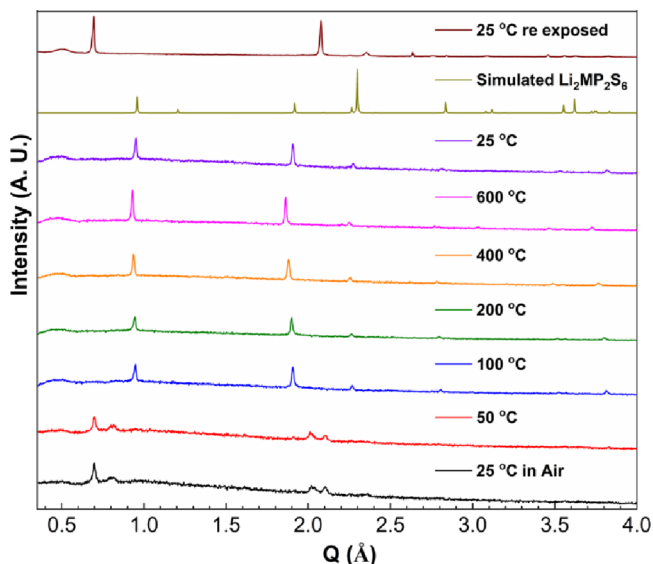


Figure 8. Thermodiffraction of $\text{Li}_2\text{MnP}_2\text{S}_6$ showing the reversible transformation from the hydrated to anhydrous phase and vice versa.

HY-I and Figures S6–S10 (for rest of the samples). The results of the thermodiffraction indicate that at $\sim 100 \text{ }^\circ\text{C}$, the hydrated structure transforms into the anhydrous phase. Interestingly, the PXRD line intensities of the compounds get progressively better due to annealing at higher temperatures.

Except for lines shifting toward slightly lower angles due to volume expansion (due to the increase in thermal vibration), no further changes are observed, indicating that the compounds are crystalline and stable until $600 \text{ }^\circ\text{C}$. Upon returning to room temperature with Ar gas flow, the samples remain in the anhydrous phase. The moment the samples are exposed to air, they transform into the hydrated phase, except in the case of **6** (Zn), where irreversible decomposition ($\text{Li}_{2.56}\text{Zn}_{0.72}\text{P}_2\text{S}_6 = \text{ZnS} + \text{uncharacterized phases}$) occurs at $600 \text{ }^\circ\text{C}$ and it does not return to the $\text{Li}_2\text{ZnP}_2\text{S}_6$ phase at room temperature (Figure S9). The structural transformation/decomposition for **6** is further confirmed by simultaneous TGA-DSC experiments (discussed below). The difference in the PXRD pattern of the air-exposed sample before and after heat treatment during the thermodiffraction experiment is due to two reasons. The first one is due to the difference in data collection procedure and exposure time of the sample to the air. Initially, the sample was briefly exposed to air and loaded into the Ar-flowing *in situ* heating chamber with a beryllium window for the first data collection (mentioned as $25 \text{ }^\circ\text{C}$ in air). After the thermodiffraction experiment, the sample was again re-exposed to air for a longer time before the data collection and without the use of the beryllium window heating chamber; it resulted in much higher intensity of peak with the emergence of new peaks that were not well resolved in the initial patterns. Second, annealing at high temperature also removes some of the stacking faults and intercalation of water in those samples may yield some well-resolved lines and even new lines. The PXRD (Figure 7b) of the 3 day air-exposed samples displays maximum extent of water intercalation by these compounds.

The structures are completely transformed into fully hydrated phases, so-called HY-II, after 3 days of exposure in air. For **1–5**, the transformation is significant as evident by the appearance of a high intensity line at much lower Q -space ($Q = 0.53 \text{ \AA}^{-1}$, $d = 11.75 \text{ \AA}$), leading to further expansion of the interlayer space in HY-II. In the case of **6**, there is no sign of hydrated phase-II; rather than developing a new line at lower Q -space, the line at $Q = 0.7 \text{ \AA}^{-1}$ moves to 0.81 \AA^{-1} and forms stable hydrated phase-I'. The nature (crystal structure) of this hydrated phase-I' is still unknown to us. Note that this phase

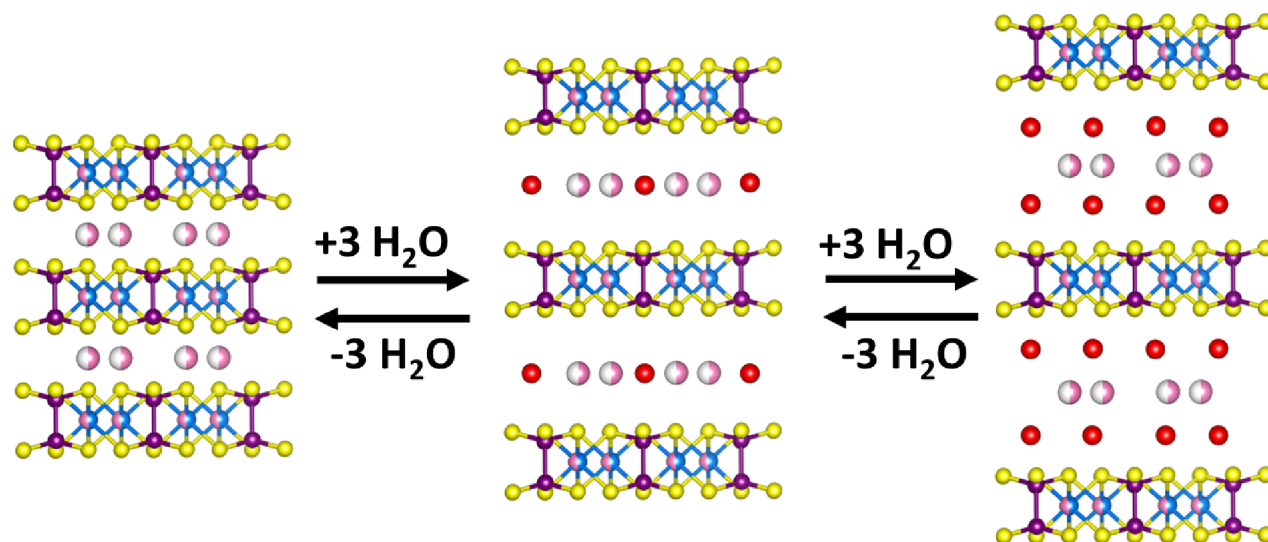


Figure 9. Schematic illustration of interlayer expansion in $\text{Li}_2\text{MP}_2\text{S}_6$ upon successive water intercalation, forming the monolayer and bilayers.

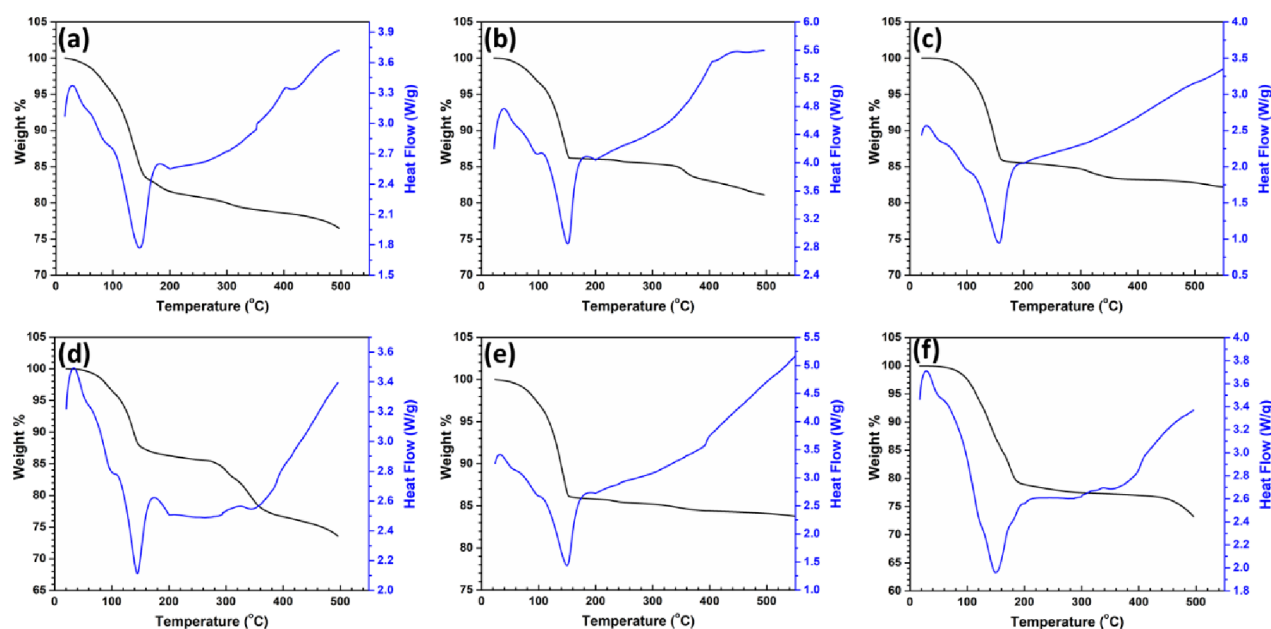


Figure 10. TGA-DSC curves of hydrated phase-I and $\text{Li}_2\text{MP}_2\text{S}_6$ exhibiting huge weight loss until 200 °C due to the loss of intercalated water molecule. (a) $M = \text{V}$ (1), (b) $M = \text{Mn}$ (2), (c) $M = \text{Fe}$ (3), (d) $M = \text{Co}$ (4), (e) $M = \text{Ni}$ (5), and (f) $M = \text{Zn}$ (6) upon water intercalation, forming the monolayer ($\text{Li}_2\text{MP}_2\text{S}_6 \cdot x\text{H}_2\text{O}$, $x \approx 3$ for all).

starts to appear in the 1 day-exposed sample with a small line at $Q = 0.81 \text{ \AA}^{-1}$. This clearly shows that except for Zn (6), where we observed one hydrated phase (monolayer), the water intercalation into the interlayer space of the structure can happen in a two-step manner, forming a monolayer (hydrated phase-I) followed by bilayer formation of water (hydrated phase-II) as supported by two endothermic peaks in DSC curves (discussed below) and akin to those vacancy-bearing $\text{M}_{1-x}\text{PS}_3\text{G}_{2x}(\text{H}_2\text{O})_y$ phases.^{17,18} Since the (00l) lines are the only most intense lines in hydrated phases, we could calculate expansion along c -axis and the interlayer d -spacing to correlate with the amount of water intercalation. The interlayer d -spacing along c -axis for anhydrous $\text{Li}_2\text{MP}_2\text{S}_6$ is $\sim 6.61 \text{ \AA}$. The hydrated phase-I with first line at $Q = 0.7 \text{ \AA}^{-1}$ has a d -spacing of 8.97 \AA with a difference of $\Delta d = 2.36 \text{ \AA}$, which approximately equals to the van der Waals diameter of a water molecule (2.7 \AA). Thus, this hydrated phase-I can be assigned with the monolayer of water molecule intercalation in the Li layer. In the case of hydrated phase-II, it is a fully hydrated phase with $Q = 0.53 \text{ \AA}^{-1}$ and a d -spacing of 11.75 \AA results into $\Delta d = 5.14 \text{ \AA}$. In the absence of a single-crystal structure solution of the fully hydrated (HY-II) phase, we hypothesize that this corresponds to a bilayer of water as shown schematically in Figure 9.

Although the exposure time is the same for all the compounds, the degree of hydration varies from sample to sample. These water intercalation reactions are classic examples of postsynthetic modification of 2D-layered chalcogenides with single crystal-to-single crystal transformation recently reviewed by Berseneva and zur Loye.³⁹

To get further insights on the amount of water intake by each sample at hydrated phase-I and phase-II and determine the thermal stability, we performed simultaneous TGA-DSC experiments. Since the hydration enthalpy of Li^+ ($\Delta H = -519 \text{ kJ/mol}$) is higher than that of any other alkali metals,⁴⁰ the samples intercalated a significant amount of water in comparison with previously reported Na^+ -based sulfides and

selenides.^{29,30,32} The TGA-DSC plots of HY-I (Figure 10) and HY-II (Figure S11) show weight loss values of $\sim 15\%$ ($\sim 3 \text{ H}_2\text{O}$) and $\sim 25\%$ ($\sim 6 \text{ H}_2\text{O}$), respectively, from room temperature to 200 °C. In hydrated phase-II, ~ 6 molecules of water per formula unit correspond to each interlayer Li satisfying 6-coordination with water as in the chemical formula $\text{Li}(\text{H}_2\text{O})_6(\text{Li}/\text{M})\text{P}_2\text{S}_6$ (Figure S11).

From the d -spacing calculation, it appears to form a bilayer of water, fully satisfying the Li coordination with water. In contrast, HY-I has water-bonded to Li in the basal plane, while Li is still interacting (weakly) with the S-donor in axial sites in trigonal prismatic coordination with $d_{(\text{Li}-\text{S})_{\text{av}}}$ of $3.52(9) \text{ \AA}$ as in the case of 2 (Mn)-HY-I. The DSC curves for HY-II (Figure S11) also show two endothermic peaks below 200 °C, indicating that the water is removed from the structure in two steps. After the initial weight loss due to water, the compounds remain stable until 600 °C, followed by a significant weight loss due to reaction with impurity oxygen in UHP argon with the sulfide surface (Figure S11). The hydrated phase-II of 4 (Co) and 6 (Zn) is quite different from the others, showing ~ 37.5 and 35% weight loss, respectively, corresponding to ~ 10 molecules of water in the structure (Figure S11c,e). It is highly likely that there are more hydrated phases besides HY-I and HY-II.

Also, 4 remains stable until 600 °C as the other compounds in the series, while 6 decomposes peritectically at $\sim 425 \text{ °C}$. This transformation was clearly visualized earlier while obtaining the thermal diffractogram of compound 6. Also, note that even for Zn-HY-I, TGA shows higher water loss ($\sim 20\%$), which is due to the emergence of another phase that we have attributed to hydrated phase-I' with no structural information.

We also performed FTIR on all the air-exposed samples (Figure 11), and the bands present around 550 and 605 cm^{-1} in all samples correspond to the asymmetric stretching^{41,42} of PS_3 , indicating the presence of the P_2S_6 building unit in the hydrated phases. All the compounds exhibit absorption bands

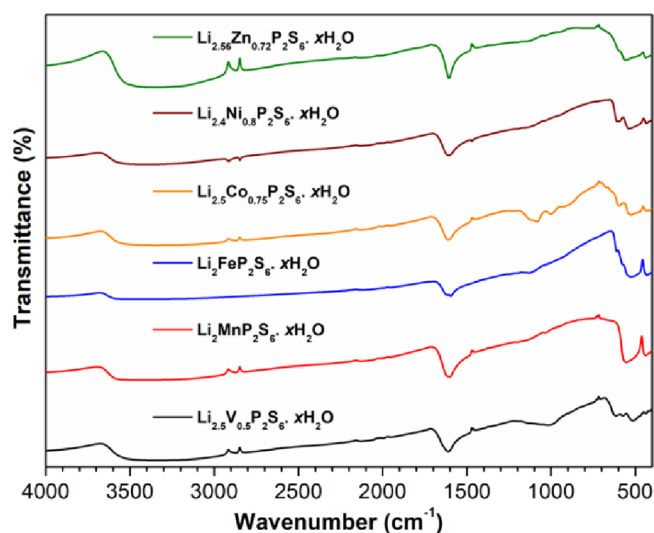


Figure 11. FTIR of hydrated $\text{Li}_2\text{MP}_2\text{S}_6 \cdot x\text{H}_2\text{O}$.

corresponding to symmetric (ν_1) and antisymmetric (ν_3)—O—H stretching centered at 3418.5 cm^{-1} and H—O—H bending modes at 1608 cm^{-1} .^{29,42} Additionally, a weak band around 2100 cm^{-1} is also observed in all samples due to the combination of bending and librational modes. These results further confirm the presence of intercalated water in the structure.

The SEM images of partially hydrated samples before and after thermogravimetric studies were acquired as a typical example to examine any occurrence of morphological changes in the structure (Figure S12). The water-intercalated samples of **6** show cracks in the layers along with slight expansion due to the swelling. The images of samples taken after thermogravimetric study show retention of cracks between the layers in the structure. The formation of two different phases in **6** is evident from the visual inspection of the color contrast in the image. This also supports the structural decomposition of $\text{Li}_{2.56}\text{Zn}_{0.72}\text{P}_2\text{S}_6$ beyond $425 \text{ }^\circ\text{C}$. It is to be noted that this decomposition of **6** at $425 \text{ }^\circ\text{C}$ is only triggered when we heat the hydrated phase.

Ammonia Intercalation. As the structure exhibited good reversibility on water intercalation, we wanted to evaluate whether insertion of NH_3 is possible in a similar manner. Ammonia intercalation into the interlayer space can regulate the physical properties of the materials as the binding of Li^+ with a nitrogen donor is stronger than an oxygen donor. To

study ammonia intercalation, first, we wanted to intercalate ammonia to fully dehydrated selected samples from moisture-free purified liquid ammonia and generate authentic IR spectra with signature absorption bands for ammonia. The details of NH_3 intercalation experiment are given in the Supporting Information. The PXRD of ammonia-intercalated samples of **1–3** and **5** shows a similar pattern as hydrated phase-I with the high intense peak at Q -spacing of 0.68 \AA^{-1} ($d = 9.23 \text{ \AA}$) for all the compounds, which is presumably a monolayer of ammonia intercalation (Figure 12a). To further confirm the presence of ammonia and rule out the ambiguity with water intercalation, FTIR spectra were collected for all four samples (Figure 12b). The peak at 3350 cm^{-1} in all the samples is attributed to the symmetric stretching of intercalated NH_3 . The NH_3 bending vibration peaks can be clearly seen at 1554 (asymmetric) and 1110 cm^{-1} (symmetric/umbrella modes), further confirming the intercalation of ammonia into the structure with interlayer expansion.⁴³ However, the degree of NH_3 intercalation slightly varies from sample to sample. TG-DSC has been used to quantify the amount of intercalated ammonia, which suggests varying degree of intercalated ammonia, $\text{Li}_2\text{MP}_2\text{S}_6 \cdot x\text{NH}_3$, $x = 2.2, 2.4, 3.1,$ and 2.2 for **1, 2, 3,** and **5**, respectively (Figure S13a–d). It is also instructive to compare the ammoniated Li intercalation in FePS_3 , leading to the composition $\text{Li}(\text{NH}_3)_x\text{FePS}_3$ reported by Feng et al.²¹ to our ammoniated phase, $\text{Li}_2\text{FeP}_2\text{S}_6 \cdot \sim 3\text{NH}_3$. To the first glance at PXRD, one can see similarity. The first line exactly coincides; however, there are subtle differences in the high angle lines both in terms of position and intensity (Figure S14). Another notable difference is that in reported $\text{Li}(\text{NH}_3)_x\text{FePS}_3$, Li is inserted reductively, lowering the oxidation state of iron from Fe^{2+} , while in the present case, it is just solvation of Li^+ in the interlamellar space of prelithiated $\text{Li}_2\text{FeP}_2\text{S}_6$ with no redox taking place. Due to its sustainable hydrogen density, NH_3 is regarded as a potential medium for hydrogen storage.⁴⁴ As a result, the reversible solid-state storage of NH_3 molecules while avoiding material corrosion is emerging as a promising field.⁴⁵ In this regard, we wanted to evaluate the selectivity of NH_3 molecule intercalation over H_2O in the interlayers, since ammonia is always contaminated with moisture. We exposed compounds **2** (Mn), **3** (Fe), and **5** (Ni) in air for 1 day to achieve the first hydrated phase (HY-I). These samples were then subjected to NH_3 gas purging for 6 h, and then the samples were recovered inside the glovebox. FTIR studies on these samples (Figure 12c) show the same characteristic peaks as observed when we intercalated the NH_3 molecule from liquid ammonia. These results further prove that these samples have higher selectivity

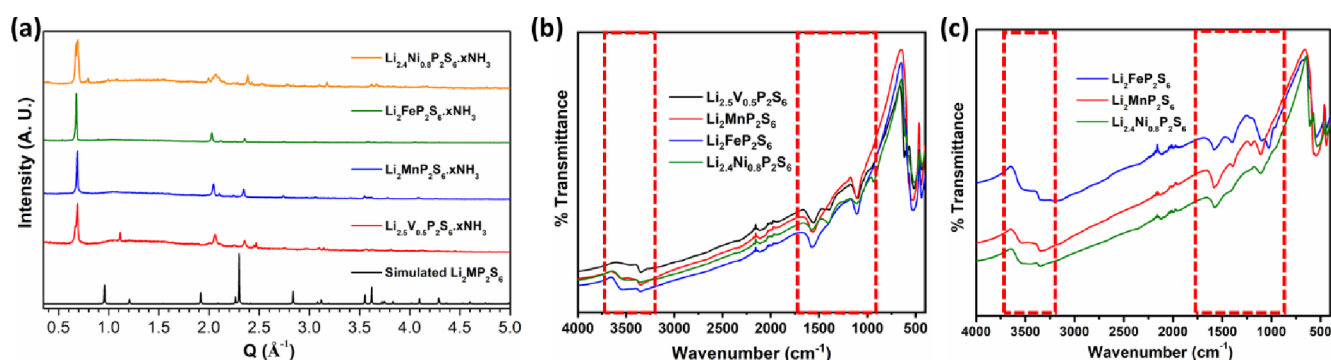


Figure 12. (a) Powder X-ray diffraction data of NH_3 -intercalated $\text{Li}_2\text{MP}_2\text{S}_6$. FTIR spectra of NH_3 -intercalated compounds via liquid ammonia (b) and via purging of ammonia gas (c).

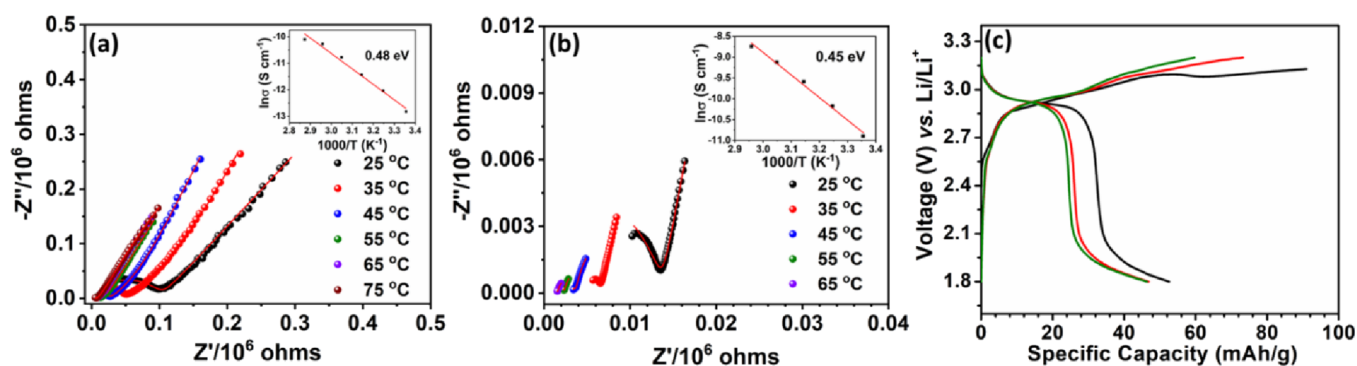


Figure 13. Nyquist plot from the AC impedance spectroscopy of (a) anhydrous $\text{Li}_{2.56}\text{Zn}_{0.72}\text{P}_2\text{S}_6$ and (b) hydrated $\text{Li}_{2.56}\text{Zn}_{0.72}\text{P}_2\text{S}_6$. (c) Charge–discharge curve of $\text{Li}_2\text{FeP}_2\text{S}_6$ at a current density of 10 mA/g.

for NH_3 molecule intercalation over H_2O . One of the likely reasons for this observation may stem from the fact that ammoniation enthalpy is slightly higher than hydration for Li^+ .^{40,46,47} The difference in IR spectra of H_2O - and NH_3 -intercalated samples are shown in Figure S15 as a typical example for the $M = \text{Mn}$ phase. Hence, the $\text{Li}_2\text{MP}_2\text{S}_6$ family of compounds with high selectivity and propensity for reversible intercalation of NH_3 molecules can potentially be a suitable class of materials for ammonia storage.

As mentioned earlier, 2D vdW thiophosphates, $\text{MPS}_3/\text{M}_2\text{P}_2\text{S}_6$, are well known for their intercalation chemistry of several guest ions and molecules such as Li, Na, K, NH_3 , pyridine, and many others. Such a variety of intercalation is possible due to the flexible van der Waals gap between the layers to host the hydrated guest species charge compensated by the removal of intralayer metal ions, $\text{M}_{1-x}\text{PS}_3\text{G}_{2x}(\text{H}_2\text{O})_y$, or through a reductive process. Through such intercalations, this class of materials exhibited a wide range of applications in optical, electrical, magnetic, and superionic conductors and energy storage fields. This wealth of literature gives us plenty of opportunities to explore the intercalation chemistry of these prelithiated thiophosphate structures with different transition metal ions, $\text{Li}_{2-x}(\text{M}_{2-x}\text{Li}_x)\text{P}_2\text{S}_6$. Additionally, this group of compounds also provides opportunity for oxidative deintercalation, which is not possible in classic vdW $\text{M}_2\text{P}_2\text{S}_6$. To the best of our knowledge, this is the first-time report of water and ammonia intercalation in the $\text{Li}_2\text{MP}_2\text{S}_6$ structure type.

Ionic Conductivity. Since we are replacing half of lithium from $\text{Li}_4\text{P}_2\text{S}_6$ by a +2 ion, it is expected that more vacancies will be created, and Li-ionic conductivity will increase. We therefore wanted to test our hypothesis by measuring the ionic conductivity of the nonredox active metal-containing compound $\text{Li}_{2.56}\text{Zn}_{0.72}\text{P}_2\text{S}_6$ (**6**). The ionic conductivity of the anhydrous and hydrated phase (**HY-I**) of **6** was measured using AC impedance spectroscopy. The Nyquist plot of the impedance spectra consists of a semicircle at the high-frequency region due to bulk resistance followed by a slope at lower frequency attributed to the charge accumulation at the blocking electrode (Figure 13a). The room-temperature ionic conductivity is calculated from the bulk resistance of the material in the Nyquist plot by fitting the spectra using the equivalent circuit given in the Supporting Information (Figure S16). As the ionic conductivity of **6** follows Arrhenius behavior with the rise in temperature, the activation energy (E_a) is calculated using the equation $\sigma_T = \sigma_0 \exp(-E_a/K_B T)$, where σ_T is the ionic conductivity, σ_0 is a pre-exponential factor, T is the absolute temperature, and k_B is the Boltzmann constant. The

room-temperature ionic conductivity of anhydrous **6** is 2.69×10^{-3} mS/cm with an activation energy of 0.48 eV. The ionic conductivity of anhydrous **6** is 4 orders of magnitude higher than that of crystalline $\text{Li}_4\text{P}_2\text{S}_6$ (1.6×10^{-7} mS/cm) at room temperature.⁴⁸ Such an increase in ionic conductivity is due to the substitution of 2Li^+ by one Zn^{2+} in $\text{Li}_4\text{P}_2\text{S}_6$, creating more vacancy or more room for the facile 2D Li^+ ion conduction path. The hydrated phase (**HY-I**) of **6** showed a much higher ionic conductivity of 1.85×10^{-2} mS/cm, which is approximately 7-fold higher than the anhydrous phase (Figure 13b) with an activation energy of 0.45 eV. The improved ionic conductivity can be explained as an effect of expanded interlayer spacing of the compound through water intercalation that facilitates better mobility of Li^+ ions. Similar cases of hydration-mediated ionic conductivity improvements have been reported recently in Na-based chalcogallates.^{29,32} It is to be noted here that while we were preparing this paper, we noticed another article reporting the ionic conductivity of $\text{Li}_{4-2x}\text{Zn}_x\text{P}_2\text{S}_6$, where they also obtained similar values of ionic conductivity.⁴⁹

Electrochemical Measurements. Li-ion coin cells were made with $\text{Li}_2\text{FeP}_2\text{S}_6$ (**3**) as a cathode and Li metal as an anode to evaluate the reversibility of electrochemical Li^+ (de)intercalation from the structure. Several MPS_3 thiophosphate-based materials have been explored as an anode, delivering high capacities through a conversion mechanism, and some are also tested as primary Li-ion cells.^{50,51} However, the prelithiated $\text{Li}_2\text{MP}_2\text{S}_6$ structure type has not been extensively explored as an intercalation cathode for Li-ion batteries. Such compositions provide the opportunity to access the $\text{M}^{2+/3+}$ redox couple at a higher voltage through the deintercalation of Li^+ from the structure. Also, in the recent times, achieving high energy density cathodes through cation and sulfide anion redox gives an opportunity for different classes of thiophosphate to be explored as a feasible cathode material.^{52,53} $\text{Li}_2\text{FeP}_2\text{S}_6$ as a cathode with an oxysulfide glass electrolyte ($\text{Li}_3\text{PO}_4\text{-Li}_2\text{S-SiS}_2$) was previously reported by Takada et al., suggesting the possibility of utilizing thiophosphate frameworks for Li-ion batteries.²⁵ However, the reversibility, long cyclability, and charge compensation mechanisms of this class of materials are yet to be understood thoroughly. To the best of our knowledge, this is the first time reporting the electrochemical performance of $\text{Li}_2\text{FeP}_2\text{S}_6$ as a cathode in Li-ion batteries using a liquid electrolyte. The first charging curve in the charge–discharge cycle shows a long flat plateau around 2.9 V until 3.2 V, attributed to 1.1 Li^+ removal from the structure (theoretical capacity for 1 Li^+ extraction is

82.7 mAh/g) (Figure 13c). Such high voltage Fe^{2+/3+} redox couple in the sulfide system is achieved through the inductive effect caused by the P₂S₆⁴⁻ polyanion moiety that pushes the Fe^{2+/3+} redox couple to higher voltage than the Fe-containing pure sulfide system.⁵³ It is also important to note that when the octahedrally coordinated Fe²⁺ *d*-band partially overlaps with the ligand, S²⁻, *p*-band in the valence band,^{25,52} it is well known that charge compensation is achieved from both cation and anion oxidation that results in the deintercalation of more than 1 Li⁺ from the structure.⁵² We do not have the electronic band structure of Li₂MP₂S₆ series of compounds; however, taking cue from the electronic band structure of vdW 2D compounds, M₂P₂S₆, the anionic redox cannot be completely ruled out as the e_g *d*-band and S *p*-band have considerable contribution at the top of the valence band, leading to a strong covalent Fe–S interaction.^{37,38} However, only 0.6 mol of Li⁺ can be reinserted at the first discharge (1.8 V), indicating that only part of the oxidized species is reversibly reduced. Such irreversibility can occur due to excessive oxidation of S²⁻ ligand that causes instability to the structural framework. On the consecutive cycles, the structure is able to sustain reversible (de)intercalation of 0.5 mol of Li⁺. Furthermore, on increasing the current density, the capacity continues to fade and could not recover the initial capacities when cycled back to the low current rates (Figure S17a). To evaluate the performance degradation, the batteries were broken at fully charged and discharged states after the first cycle and washed with acetonitrile (ACN) before performing ex situ PXRD. To our surprise, both fully charged and discharged samples are completely transformed into the solvated phase similar to the H₂O and NH₃ intercalation scenarios (Figure S17b). However, it is also worth noticing that the peaks of the pristine compound are still intact, which means that part of the cathode has intercalated solvent molecules and, in this case, it can either be ACN (during electrode washing) or could be from the electrolyte solvent (EC/DMC-solvated Li⁺) during electrochemical charge–discharge. To evaluate these hypotheses, we soaked two pristine cathode films into the Li-ion electrolyte and ACN for 1 day inside the glovebox and PXRD was collected (Figure S17c). The lines in the PXRD pattern of the electrolyte-soaked cathode are broadened at the lower angle with reduced observed intensities for the remaining peaks with no clear lattice expansion. On the other hand, the ACN-soaked sample was transformed into the solvated phase with a low angle peak at *Q* = 7 Å⁻¹. Since both reactions were performed inside the glovebox (O₂ < 0.1 ppm and H₂O < 0.1 ppm), we do not expect such a change in the powder pattern due to hydration. So, we attribute such a change in PXRD to solvent intercalation into the layers of compound 2; still, more detailed studies have to be carried out to verify the possibilities of such solvent molecule intercalations. Also, note that Takada et al. reported the first Li-ion battery using Li₂FeP₂S₆ as a cathode where they have shown one cycle of charge–discharge with similar capacity without any mention on the fate of the cathode.²⁵ We are currently working on understanding the origin of capacity fading and prospect of carbonate and polymer molecule intercalation into the structure. Recently, during our preparation of the paper, we came across a work where a solid-state Li-ion battery has been fabricated using Li₂FeP₂S₆ as a cathode, but the achievable capacity is very similar to this work.⁵⁴

CONCLUSIONS

A series of non-vdW layered solids, Li₂MP₂S₆ (M = V, Mn, Fe, Co, Ni, and Zn), has been successfully synthesized through stoichiometric combination of metal powder, Li₂S and P₂S₅, and metathesis routes (for V, Mn, Fe, Ni, and Zn). The crystal structure solution of the anhydrous phases through single-crystal and synchrotron X-ray diffraction studies reveals 2D layers of [Li/MP₂S₆]⁻ interleaved by Li ions. PXRD, thermodiffraction, and TG-DSC on the compounds show propensity for reversibly intercalated water, leading to two distinct hydrated phases. The compounds also display affinity toward NH₃ intercalation over water in their interlayer space. The magnetic measurements on Li₂MP₂S₆ (M = Mn and Ni) performed for the first time show paramagnetic behavior down to 2 K without any magnetic transition. The AC impedance measurements of anhydrous Li_{2.56}Zn_{0.72}P₂S₆ display significantly improved ionic conductivity compared to Li₄P₂S₆. Electrochemical testing on Li₂FeP₂S₆ reveals topotactic oxidative deintercalation and reductive insertion of Li⁺ during charge–discharge cycles. This new class of thiophosphate materials with interesting intercalation property can find application as an adsorbent, electrode materials, and solid electrolyte besides being excellent candidates for fundamental studies in low dimensions through exfoliated layers.

ASSOCIATED CONTENT

Supporting Information

The Supporting Information is available free of charge at <https://pubs.acs.org/doi/10.1021/acs.chemmater.3c02829>.

Detailed experimental information on ammonia intercalation, diffraction, ICP, spectroscopy, microscopy, TGA, magnetic measurements, battery fabrication, and ionic conductivity; figures of metathesis reaction with Li₄P₂S₆ and CoCl₂; synchrotron PXRD of hydrated phase-I of Li₂MnO₃P₂S₆; DRS spectra of Li₂MP₂S₆; thermodiffractiongrams of Li₂MP₂S₆; TGA of Li₂MP₂S₆ after 3 days of exposure to air; SEM images of Li_{2.56}Zn_{0.72}P₂S₆; TGA, and PXRD of NH₃-intercalated compounds; equivalent circuit, and fitting parameters of Li_{2.56}Zn_{0.72}P₂S₆; capacity retention curve and PXRD after electrochemical cycles of Li₂FeP₂S₆; table of crystal structure data and refinement parameters of Li₂MnP₂S₆ and Li₂MnO_{2.48}P₂S₆; table of atomic coordinates of Li₂MP₂S₆ (M = V, Mn, Co, and Ni); Rietveld refinement of Li₂MnO₃P₂S₆; table of Li/M ratio from ICP-OES and optical band gap of Li₂MP₂S₆ (M = V, Mn, Fe, Co, Ni, and Zn) (PDF)

AUTHOR INFORMATION

Corresponding Author

Amitava Choudhury – Department of Chemistry, Missouri University of Science and Technology, Rolla, Missouri 65409, United States; orcid.org/0000-0001-5496-7346; Email: choudhurya@mst.edu

Authors

Santhoshkumar Sundaramoorthy – Department of Chemistry, Missouri University of Science and Technology, Rolla, Missouri 65409, United States; orcid.org/0000-0001-5037-0016

Nikolay Gerasimchuk – Department of Chemistry and Biochemistry, Blunt Hall 456, Missouri State University,

Springfield, Missouri 654897, United States; orcid.org/0000-0003-4867-6475

Kartik Ghosh – Department of Physics, Missouri State University, Springfield, Missouri 65897, United States
Steven P. Kelley – Department of Chemistry, University of Missouri, Columbia, Missouri 65211, United States;
orcid.org/0000-0001-6755-4495

Complete contact information is available at:
<https://pubs.acs.org/10.1021/acs.chemmater.3c02829>

Notes

The authors declare no competing financial interest.

ACKNOWLEDGMENTS

A.C. and S.S. acknowledge the funding from the National Science Foundation (DMR-1809128). Use of Advanced Photon Source at Argonne National Laboratory was supported by the U.S. Department of Energy, Office of Science, Office of Basic Energy Sciences, under contract no. DE-AC02-06CH11357. N.G. is grateful to the MSU CNAS and the Department of Chemistry and Biochemistry for continuous support and repairs of thermal analysis equipment.

REFERENCES

- Brec, R. Review on Structural and Chemical Properties of Transition Metal Phosphorous Trisulfides MPS₃. *Solid State Ion.* **1986**, *22* (1), 3–30.
- Brec, R.; Schleich, D. M.; Ouvrard, G.; Louisy, A.; Rouxel, J. Physical Properties of Lithium Intercalation Compounds of the Layered Transition-Metal Chalcogenophosphites. *Inorg. Chem.* **1979**, *18* (7), 1814–1818.
- Joy, P. A.; Vasudevan, S. Magnetism in the Layered Transition-Metal Thiophosphates MPS₃ (M = Mn, Fe, and Ni). *Phys. Rev. B* **1992**, *46* (9), 5425–5433.
- Synnatschke, K.; van Dinter, J.; Müller, A.; Tiede, D.; Spillecke, L.; Shao, S.; Kelly, D.; Konecny, J.; Konkena, B.; McCrystal, M.; Saigal, N.; Wurstbauer, U.; Bensch, W.; Sofer, Z.; Coleman, J. N.; Klingeler, R.; Haigh, S. J.; Backes, C. Exfoliability, Magnetism, Energy Storage and Stability of Metal Thiophosphate Nanosheets Made in Liquid Medium. *2D Mater.* **2023**, *10* (2), No. 024003.
- Susner, M. A.; Chyasnachyus, M.; McGuire, M. A.; Ganesh, P.; Maksymovych, P. Metal Thio- and Selenophosphates as Multifunctional van der Waals Layered Materials. *Adv. Mater.* **2017**, *29* (38), No. 1602852.
- Lee, J.-U.; Lee, S.; Ryoo, J. H.; Kang, S.; Kim, T. Y.; Kim, P.; Park, C.-H.; Park, J.-G.; Cheong, H. Ising-Type Magnetic Ordering in Atomically Thin FePS₃. *Nano Lett.* **2016**, *16* (12), 7433–7438.
- Kim, K.; Lim, S. Y.; Lee, J.-U.; Lee, S.; Kim, T. Y.; Park, K.; Jeon, G. S.; Park, C.-H.; Park, J.-G.; Cheong, H. Suppression of Magnetic Ordering in XXZ-Type Antiferromagnetic Monolayer NiPS₃. *Nat. Commun.* **2019**, *10* (1), 345.
- Bai, W.; Hu, Z.; Xiao, C.; Guo, J.; Li, Z.; Zou, Y.; Liu, X.; Zhao, J.; Tong, W.; Yan, W.; Qu, Z.; Ye, B.; Xie, Y. Parasitic Ferromagnetism in Few-Layered Transition-Metal Chalcogenophosphate. *J. Am. Chem. Soc.* **2020**, *142* (24), 10849–10855.
- Liang, Q.; Zheng, Y.; Du, C.; Luo, Y.; Zhang, J.; Li, B.; Zong, Y.; Yan, Q. General and Scalable Solid-State Synthesis of 2D MPS₃ (M = Fe, Co, Ni) Nanosheets and Tuning Their Li/Na Storage Properties. *Small Methods* **2017**, *1* (12), No. 1700304.
- van Dinter, J.; Synnatschke, K.; Engesser, T. A.; Indris, S.; Wolff, N.; Gronenberg, O.; Etter, M.; Cibir, G.; Kienle, L.; Backes, C.; Bensch, W. What Happens Structurally and Chemically during Sodium Uptake and Release by Ni₂P₂S₆: A Combined X-Ray Diffraction, X-Ray Absorption, Pair Distribution Function and MAS NMR Analysis. *J. Mater. Chem. A* **2020**, *8* (42), 22401–22415.
- Yang, X.; Luo, Y.; Li, J.; Wang, H.; Song, Y.; Li, J.; Guo, Z. Tuning Mixed Electronic/Ionic Conductivity of 2D CdPS₃ Nanosheets as an Anode Material by Synergistic Intercalation and Vacancy Engineering. *Adv. Funct. Mater.* **2022**, *32* (18), No. 2112169.
- Hahn, H.; Kligen, W. Über Einige Ternäre Verbindungen Vom Typ Des Arsenopyrits. *Naturwissenschaften* **1965**, *52* (17), 494–494.
- Kligen, W.; Ott, R.; Hahn, H. Über Die Darstellung Und Eigenschaften von Hexathio- Und Hexaselenohypodiphosphaten. *Z. Anorg. Allg. Chem.* **1973**, *396* (3), 271–278.
- Ouvrard, G.; Brec, R.; Rouxel, J. Structural Determination of Some MPS₃ Layered Phases (M = Mn, Fe, Co, Ni and Cd). *Mater. Res. Bull.* **1985**, *20* (10), 1181–1189.
- Lacroix, P. G.; Clément, R.; Nakatani, K.; Zyss, J.; Ledoux, I. Stilbazolium-MPS₃ Nanocomposites with Large Second-Order Optical Nonlinearity and Permanent Magnetization. *Science* **1994**, *263* (5147), 658–660.
- Lagadic, I.; Lacroix, P. G.; Clément, R. Layered MPS₃ (M = Mn, Cd) Thin Films as Host Matrixes for Nonlinear Optical Material Processing. *Chem. Mater.* **1997**, *9* (9), 2004–2012.
- Clement, R. A Novel Route to Intercalation into Layered MnPS₃. *J. Chem. Soc., Chem. Commun.* **1980**, *14*, 647–648.
- Clement, R.; Garnier, O.; Jegoudez, J. Coordination Chemistry of the Lamellar MPS₃ Materials: Metal-Ligand Cleavage as the Source of an Unusual “Cation-Transfer” Intercalation Process. *Inorg. Chem.* **1986**, *25* (9), 1404–1409.
- Qian, X.; Chen, L.; Yin, L.; Liu, Z.; Pei, S.; Li, F.; Hou, G.; Chen, S.; Song, L.; Thebo, K. H.; Cheng, H.-M.; Ren, W. CdPS₃ Nanosheets-Based Membrane with High Proton Conductivity Enabled by Cd Vacancies. *Science* **2020**, *370* (6516), 596–600.
- Evans, J. S. O.; O’Hare, D.; Clement, R. The Structure of Co(η-C₅H₅)₂⁺ and NMe₄⁺ Intercalates of MnPS₃: An X-Ray, Neutron-Diffraction, and Solid-State NMR Study. *J. Am. Chem. Soc.* **1995**, *117* (16), 4595–4606.
- Feng, X.; Guo, Z.; Yan, X.; Deng, J.; Wu, D.; Zhang, Z.; Sun, F.; Yuan, W. A(NH₃)_xFePS₃ (A = Li, K): Intercalated Fe Thiophosphate via the Liquid Ammonia Method. *Mater. Chem. Front.* **2021**, *5* (6), 2715–2723.
- Balijapelly, S.; Ghosh, K.; Chernatynskiy, A. V.; Choudhury, A. Discovery of an Olivine-Type Lithium Manganese Thiophosphate, LiMnPS₄, via a Building Block Approach. *Chem. Commun.* **2021**, *57* (97), 13182–13185.
- Balijapelly, S.; Craig, A. J.; Bin Cho, J.; Jang, J. I.; Ghosh, K.; Aitken, J. A.; Chernatynskiy, A. V.; Choudhury, A. Building-Block Approach to the Discovery of Na₈Mn₂(Ge₂Se₆)₂: A Polar Chalcogenide Exhibiting Promising Harmonic Generation Signals with a High Laser-Induced Damage Threshold. *J. Alloys Compd.* **2022**, *900*, No. 163392.
- Takada, K.; Inada, T.; Kajiyama, A.; Sasaki, H.; Kondo, S.; Watanabe, M.; Kanda, M. Lithium Ion Conduction in Lithium Magnesium Thio-Phosphate. *Solid State Ion.* **2002**, *147* (1–2), 23–27.
- Takada, K.; Michiue, Y.; Inada, T.; Kajiyama, A.; Kouguchi, M.; Kondo, S.; Watanabe, M.; Tabuchi, M. Lithium Iron Thio-Phosphate: A New 3 V Sulfide Cathode. *Solid State Ion.* **2003**, *159* (3–4), 257–263.
- Schoop, L. M.; Eger, R.; Pielhofer, F.; Schneider, C.; Nuss, J.; Lotsch, B. V. Synthesis and Characterization of Three New Lithium-Scandium Hexathiohypodiphosphates: Li_{4–3x}Sc_xP₂S₆ (x = 0.358), m-LiScP₂S₆, and t-LiScP₂S₆. *Z. Anorg. Allg. Chem.* **2018**, *644* (24), 1854–1862.
- Diethrich, T. J.; Zavalij, P. Y.; Gnewuch, S.; Rodriguez, E. E. Orbital Contribution to Paramagnetism and Noninnocent Thiophosphate Anions in Layered Li₂MP₂S₆ Where M = Fe and Co. *Inorg. Chem.* **2021**, *60* (14), 10280–10290.
- Mercier, R.; Malugani, J. P.; Fahys, B.; Douglange, J.; Robert, G. Synthèse, Structure Cristalline et Analyse Vibratoire de l’hexathiohypodiphosphate de Lithium Li₄P₂S₆. *J. Solid. State Chem.* **1982**, *43* (2), 151–162.

- (29) Adhikary, A.; Yaghoobnejad Asl, H.; Sandineni, P.; Balijapelly, S.; Mohapatra, S.; Khatua, S.; Konar, S.; Gerasimchuk, N.; Chernatynskiy, A. V.; Choudhury, A. Unusual Atmospheric Water Trapping and Water Induced Reversible Restacking of 2D Gallium Sulfide Layers in NaGaS₂ Formed by Supertetrahedral Building Unit. *Chem. Mater.* **2020**, *32* (13), 5589–5603.
- (30) Klepov, V. V.; Berseneva, A. A.; Pace, K. A.; Kocevski, V.; Sun, M.; Qiu, P.; Wang, H.; Chen, F.; Besmann, T. M.; Loye, H. NaGaS₂: An Elusive Layered Compound with Dynamic Water Absorption and Wide-Ranging Ion-Exchange Properties. *Angew. Chem., Int. Ed.* **2020**, *59* (27), 10836–10841.
- (31) Joos, M.; Schneider, C.; Münchinger, A.; Moudrakovski, I.; Usiskin, R.; Maier, J.; Lotsch, B. V. Impact of Hydration on Ion Transport in Li₂Sn₂S₅·xH₂O. *J. Mater. Chem. A* **2021**, *9* (30), 16532–16544.
- (32) Balijapelly, S.; Sundaramoorthy, S.; Mondal, D. J.; Konar, S.; Gerasimchuk, N.; Chernatynskiy, A.; Choudhury, A. NaGaSe₂: A Water-Loving Multifunctional Non-van Der Waals Layered Selenogallate. *Inorg. Chem.* **2023**, *62* (9), 3886–3895.
- (33) Toby, B. H.; Von Dreele, R. B. GSAS-II: The Genesis of a Modern Open-Source All Purpose Crystallography Software Package. *J. Appl. Crystallogr.* **2013**, *46* (2), 544–549.
- (34) Du, K.; Wang, X.; Liu, Y.; Hu, P.; Utama, M. I. B.; Gan, C. K.; Xiong, Q.; Kloc, C. Weak Van Der Waals Stacking, Wide-Range Band Gap, and Raman Study on Ultrathin Layers of Metal Phosphorus Trichalcogenides. *ACS Nano* **2016**, *10* (2), 1738–1743.
- (35) Patel, S.; Balchin, A. A Correction to Preparation and Structural Studies of Lithium-Substituted Nickel Phosphorus Trisulphide, Li₂NiP₂S₆ Solid State Ionics 14 (1984) 45–49. *Solid State Ion.* **1986**, *20* (3), 223–224.
- (36) Atkins, P.; Overton, T.; Rourke, J.; Weller, M.; Armstrong, F. *Inorganic Chemistry*, Fifth Edit.; Oxford University Press: New York, 2010.
- (37) Whangbo, M. H.; Brec, R.; Oувrard, G.; Rouxel, J. Reduction Sites of Transition-Metal Phosphorus Trichalcogenides MPX₃. *Inorg. Chem.* **1985**, *24* (15), 2459–2461.
- (38) Mercier, H.; Mathey, Y.; Canadell, E. On the Electronic Structure of MPS₃ Phases. *Inorg. Chem.* **1987**, *26* (6), 963–965.
- (39) Berseneva, A. A.; zur Loye, H.-C. Advances in Chalcogenide Crystal Growth: Flux and Solution Syntheses, and Approaches for Postsynthetic Modifications. *Cryst. Growth Des.* **2023**, *23* (8), 5368–5383.
- (40) Smith, D. W. *Ionic Hydration Enthalpies*. *J. Chem. Edu.* **1977**, *54* (9), 540.
- (41) Jeevanandam, P.; Vasudevan, S. Conductivity and Dielectric Response in the Ion-Exchange Intercalated Mono- and Double-Layer Hydrates Cd_{0.75}PS₃Na_{0.5}(H₂O)_y, y = 1, 2. *J. Phys. Chem. B* **1998**, *102* (17), 3082–3089.
- (42) Mathey, Y.; Clement, R.; Sourisseau, C.; Lucazeau, G. Vibrational Study of Layered MPX₃ Compounds and of Some Intercalates with Co(η⁵-C₅H₅)₂⁺ or Cr(η⁶-C₆H₆)₂⁺. *Inorg. Chem.* **1980**, *19* (9), 2773–2779.
- (43) Frink, K. J.; Wang, R. C.; Colon, J. L.; Clearfield, A. Intercalation of Ammonia into Zinc and Cobalt Phenylphosphonates. *Inorg. Chem.* **1991**, *30* (7), 1438–1441.
- (44) Han, X.; Lu, W.; Chen, Y.; da Silva, I.; Li, J.; Lin, L.; Li, W.; Sheveleva, A. M.; Godfrey, H. G. W.; Lu, Z.; Tuna, F.; McInnes, E. J. L.; Cheng, Y.; Daemen, L. L.; MPherson, L. J. M.; Teat, S. J.; Frogley, M. D.; Rudić, S.; Manuel, P.; Ramirez-Cuesta, A. J.; Yang, S.; Schröder, M. High Ammonia Adsorption in MFM-300 Materials: Dynamics and Charge Transfer in Host–Guest Binding. *J. Am. Chem. Soc.* **2021**, *143* (8), 3153–3161.
- (45) Zhang, T.; Miyaoka, H.; Miyaoka, H.; Ichikawa, T.; Kojima, Y. Review on Ammonia Absorption Materials: Metal Hydrides, Halides, and Borohydrides. *ACS Appl. Energy Mater.* **2018**, *1* (2), 232–242.
- (46) Senozan, N. M. Effective Ionic Radii and the Enthalpies of Solvation in Liquid Ammonia. *J. Inorg. Nucl. Chem.* **1973**, *35* (3), 727–736.
- (47) Coulter, L. V. The Thermochemistry of the Alkali and Alkaline Earth Metals and Halides in Liquid Ammonia at – 33°. *J. Phys. Chem.* **1953**, *57* (6), 553–558.
- (48) Dietrich, C.; Sadowski, M.; Sicolo, S.; Weber, D. A.; Sedlmaier, S. J.; Weldert, K. S.; Indris, S.; Albe, K.; Janek, J.; Zeier, W. G. Local Structural Investigations, Defect Formation, and Ionic Conductivity of the Lithium Ionic Conductor Li₄P₂S₆. *Chem. Mater.* **2016**, *28* (23), 8764–8773.
- (49) Lyoo, J.; Kim, H. J.; Hyoung, J.; Chae, M. S.; Hong, S.-T. Zn Substituted Li₄P₂S₆ as a Solid Lithium-Ion Electrolyte for All-Solid-State Lithium Batteries. *J. Solid State Chem.* **2023**, *320*, No. 123861.
- (50) Wang, F.; Shifa, T. A.; Yu, P.; He, P.; Liu, Y.; Wang, F.; Wang, Z.; Zhan, X.; Lou, X.; Xia, F.; He, J. New Frontiers on van Der Waals Layered Metal Phosphorus Trichalcogenides. *Adv. Funct. Mater.* **2018**, *28* (37), No. 1802151.
- (51) Kuzminskii, Y. V.; Voronin, B. M.; Redin, N. N. Iron and Nickel Phosphorus Trisulfides as Electroactive Materials for Primary Lithium Batteries. *J. Power Sources* **1995**, *55* (2), 133–141.
- (52) Saha, S.; Assat, G.; Sougrati, M. T.; Foix, D.; Li, H.; Vergnet, J.; Turi, S.; Ha, Y.; Yang, W.; Cabana, J.; Rousse, G.; Abakumov, A. M.; Tarascon, J. M. Exploring the Bottlenecks of Anionic Redox in Li-Rich Layered Sulfides. *Nat. Energy* **2019**, *4* (11), 977–987.
- (53) Hansen, C. J.; Zak, J. J.; Martinolich, A. J.; Ko, J. S.; Bashian, N. H.; Kaboudvand, F.; Van Der Ven, A.; Melot, B. C.; Nelson Weker, J.; See, K. A. Multielectron, Cation and Anion Redox in Lithium-Rich Iron Sulfide Cathodes. *J. Am. Chem. Soc.* **2020**, *142* (14), 6737–6749.
- (54) Zarabadi-Poor, P.; Lim, J.; Wang, X.; Bocarsly, J. D.; Daniels, L. M.; Pateli, I. M.; Chen, R.; Claridge, J. B.; Grey, C. P.; Morgan, B. J.; Hardwick, L. J.; Rosseinsky, M. J.; Islam, M. S. Accessing Polymeric Redox in High Voltage Li-Rich Thiophosphates. *ChemRxiv*, 21 February **2023**, Version 1 DOI: 10.26434/chemrxiv-2023-rl5ll (accessed 2023–03–23).